Thermal coupling optimization of bridge environmental impact under natural conditions

10728 words

ZHOU, Z.; ZHOU, J.; ALCALÁ, J.; YEPES, V. (2024). Thermal coupling optimization of bridge environmental impact under natural conditions. Environmental Impact Assessment Review, 104:107316. DOI:10.1016/j.eiar.2023.107316

ABSTRACT

Infrastructure is a crucial aspect of promoting worldwide economic integration. However, the construction of infrastructure often results in high energy consumption and substantial emissions of greenhouse gases. Over time, the environment can also cause significant damage to bridges, leading to repeated repairs and replacements that further harm the environment. This research aims to minimize the environmental impact of bridge maintenance over a 100-year lifespan. The study utilizes a three-dimensional dynamic thermo-mechanical optimization model developed through comprehensive research and interdisciplinary collaboration in various fields such as Bibliometrics, Fluid Mechanics, Structural Dynamics, Thermoelectricity, and Damage Mechanics. From examining single crystal structures at a microscopic level to examining system components under extreme temperatures, this study provides a system for reducing environmental pollution. The model's reliability is shown through a case study, demonstrating a reduction of 49.9 million tonnes of emissions, equivalent to 1.91% of total design emissions, over a 100-year maintenance period. This research provides a foundation for future studies and presents an approach for evaluating the environmental impact of long-term temperature changes in structures.

Keywords: Construction industry; Structure; Temperature; Topology Optimization; Stress; Sensitivity

Corresponding author.

1. Introduction

The alterations in structural deformation and internal forces during bridge management and maintenance reveal the structural rigidity and load response, which impact not only the longevity of the structure but also its deterioration and degradation of material properties (Deraemaeker and Worden, 2018). Vehicle loads and temperature fluctuations predominantly cause vertical deflection in bridges, and a clear linear relationship exists between the structure and temperature changes (Jayaseelan et al., 2019). Studies have revealed that the cyclical variation of ambient temperature can lead to significant deformation in long-span bridges during their service life, surpassing deformation caused by regular traffic or wind loads (Zamarrón-Mieza et al., 2017). At the same, a thermal expansion of the structure due to the internal heat conduction of structural components made of various materials exposed to sunlight. Constraining the internal force of the structure generates the "temperature gradient" effect, altering the structure's dynamic characteristics. Thus, temperature effects must be considered during the design, construction, and maintenance phases (Zhou et al., 2020).

Research innovation has focused on understanding the impact of ambient temperature on the mechanical properties, damage, and material aging of structural bridge components (Sun et al., 2020). Although much research has been carried out in this field, further research on the life cycle assessment (LCA) data of bridges exposed to ambient temperature for a long time still needs to be strengthened. The damage caused by ambient temperature to the structure's durability has significantly reduced its service life (Zhou et al., 2020). An accurate assessment of this impact and methods for reducing its cycle is essential. The bridge environmental impact theory has been established based on a coupled analysis of the structure's ambient temperature and damage models in the paper. A high-resolution finite element three-dimensional (3D) model of the bridge thermal environment has been systematically established to analyse the environmental impact data of the bridge during its 100-year service period. This interdisciplinary research has effectively realized the cross-coupling application of advanced mathematics, structural dynamics, fluid mechanics, and environmental engineering science. The research system and theoretical model apply to the coupled analysis of ambient temperature in the construction industry, contributing to further advancements in this field. Furthermore, according to LCA data, the maintenance phase is associated with reduced emissions of 49.93 million tonnes (**t**) and decreased global warming by 0.28 million t.

This paper is divided into five parts. In the Introduction, the status of the field, existing issues, and advancements in relevant publications are evaluated. The literature review analyzes the current research situation in relevant fields and proves a research gap. The Methodology section outlines a comprehensive research theoretical model framework. The Results section showcases the 3D finite element coupling analysis of a case study and the structural Thermo-mechanical Coupled Structures (TOSS) analysis. The Discussion evaluates the optimization of the 100-year environmental impact data of the bridge through TOSS analysis. Finally, the Conclusions summarize the research findings, highlight the significance of the research, and outline future research goals in this field.

2. Literature review

This paper conducts a comprehensive literature review across four research fields to ascertain the current research status, identify future development trends, and pinpoint improvement areas within this field.

2.1 Impact of temperature on bridges

The dynamic characteristics of a structure are primarily influenced by the ambient temperature, which affects both the physical and mechanical properties of materials, such as Poisson's ratio and elastic modulus and the geometric characteristics of the structure, such as boundary conditions and component dimensions (Zhou et al., 2020). Yue et al. (2022) investigated the time lag of temperature and deflection in the heat transfer process of a cable-stayed bridge

and the inertial effect of the spatial and temporal distribution of the temperature field. Quantitative research on the complex temperature deformation of cable-stayed bridges with statically indeterminate structures often uses regression and finite element analysis, which require long-term measured data, detailed design data, and professional knowledge (Xu et al., 2020). Moreover, the regularity of the ambient temperature affects the structural modal parameters, and changes in the structure's dynamic characteristics, state, response, and modal parameters can weaken the bridge-bearing capacity, leading to long-term structural damage (Lee et al., 2019; Pons et al., 2018). Therefore, it is crucial to assess the structural response characteristics caused by daily and seasonal temperature changes, analyse the response of bridge structures in the natural temperature field, and consider the environmental impact of long-term exposure to a particular environment. This study does not consider the impact of a specific environment on structural erosion (Navarro et al., 2018).

The current study faces several challenges. Firstly, due to the complex configuration and vast system of bridge structures, it is challenging to establish a global heat transfer analysis model that considers the temperature distribution and response (Xia et al., 2013). Secondly, there is room for improvement in the 3D study of the dynamic mechanical characteristics of the entire bridge under ambient temperature. Complete solid finite element modeling is challenging due to the multi-modal parameters and extensive element modeling, which negatively affects the efficiency and accuracy of optimized analysis, as suggested by Liu and Zhang (2017). Lastly, 95% of published literature collects response data through bridge health monitoring systems, which limits the scope of analysis to the bridge maintenance period and needs more timeliness and efficacy, according to He et al. (2021).

The conclusion is drawn through literature research: the study of this field has shown a downward trend in recent years, with the research hotspots and trends developing toward an interdisciplinary direction, as shown in Extended Fig. 1(a; b) and Extended Table 1. Temperature effect, heat transfer, and material properties remain hotspots.

2.2 Status of bridge topology optimization

Topology optimization refers to determining the optimal structural layout of materials while considering load actions and boundary constraints to achieve a particular property index (Briseghella et al., 2013). When designing bridge structures, the ambient temperature must be considered during operation. To address this issue, the thermal load must be considered during the Topology Optimization of TOSS. Various research models are available for this purpose, including mean TOSS, variable density method, multi-objective integrated design method, and the effect of a single material in an uneven temperature field (Kutylowski and Rasiak, 2014). Although many achievements have been published in this field, challenging research problems still exist, particularly in 3D research on the thermo-elastic oscillation of structures in natural uneven temperature fields (Meng et al., 2021).

There are some problems related to the topology optimization of long-span bridges. Firstly, how can the author solve the ubiquitous TOSS problem and optimize the structure's composition, convergence, and stability while processing a large amount of computational data? Secondly, most literature studies rely on plate, shell, and rod elements, reducing the structure's element dimension and precision. However, using a 3D solid research model can more accurately reflect the refinement and robustness of component optimization (Atmaca et al., 2022; Zhou et al., 2022).

The conclusion is drawn through literature research: a discrete sin Q fitting analysis was conducted for the nine most vital data groups, and the conclusion was consistent with that of the mutual information algorithm (Extended Figs. 1(c; d) and Extended Table 1).

2.3 Environment assessment in the construction industry

Climate change is a significant impediment to sustainable development. The European Union aims to decrease

greenhouse gas emissions by 55% and 80% by 2030 and 2050 (Dräger and Letmathe, 2022), respectively, while China plans to achieve a carbon emission peak in 2030 and carbon neutrality by 2060 to mitigate climate warming (Fu et al., 2020). However, the current situation is that industrial facilities in the United States generate 7.6 billion t of waste and emit 6.587 billion t of CO_2 annually, accounting for 21% of the total greenhouse gas emissions in 2017. The construction industries in Europe contribute 40% of the total energy consumption, 32% of the total CO_2 emissions, and 25% of the waste generated yearly (Carvalho et al., 2019). Moreover, the greenhouse gas emissions of the construction industry in the UK account for 50% of the total emissions, and the construction industry has been identified as the most emission-intensive industry. China's construction industry is also among the top three in the world in terms of annual greenhouse gas emissions (Zhou et al., 2020).

The industry must overcome the challenges of various uncertain factors to achieve sustainable economic, environmental, and social development throughout the life cycle of construction projects. The Environmental Kuznets Curve highlights the complex relationship between the three indices and the dynamic causal relationship between them (Molina-Moreno et al., 2017).

The Life Cycle Assessment (LCA) process is divided into four parts: objective and scope definition, life cycle inventory analysis, impact assessment, and interpretation. The study covers the five stages of the "cradle to grave" cycle, planning and design, material manufacturing and transportation, construction, maintenance and operation, and waste management (Ma et al., 2021).

Two main issues need to be addressed regarding the environmental impact of bridges. Firstly, there needs to be sufficient literature on LCA studies for bridges, especially regarding the impact of long-term natural climate change, such as changes in ambient temperature, on their service life. Secondly, there is a need to investigate the environmental impact caused by climate and temperature changes during the 100-year operational period of bridges.

The conclusion is drawn through literature research: there are many research papers on LCA worldwide, the overall research direction remains unchanged, and the scope of research content and fields is gradually expanding (Extended Figs. 1(e; f) and Extended Table 1).

2.4 Damage response of thermal stress coupled

Bridges are primarily constructed with concrete and steel, both subject to mechanical stresses when exposed to temperature changes. During the operational period, the load on the bridge causes minor defects such as cracks and damages to develop due to the destructive effects of concrete's heat transfer and diffusion. Thermal conductivity is associated with specific heat capacity. In a study by Duc Tho Pham (Penadés-Plà et al., 2019; Pham et al., 2021), the Absar Plot data analysis was used to examine the crack initiation and propagation model resulting from temperature-related substantial damage (see Extended Fig. 1(g)).

The defect formation mechanism is that the structure's transverse reinforcement bears a hefty load capacity whose strength surpasses the viscous resistance between the reinforcement surface and the concrete. Over time, this results in transverse and longitudinal splitting cracks around the reinforcement, which break through the concrete protective layer under continuous radial expansion, leading to component cracking and deformation (Sharma et al., 2019). Additionally, the strength and adhesion performance of the structure's skeleton is reduced under long-term cyclic ambient temperature conditions (Extended Fig. 1(h)).

Two central problems in the field of bridge engineering require further attention. Firstly, it is essential to understand how static and dynamic loads and long-term temperature changes affect bridge components' maintenance and design life. Accurately assessing the impact data is crucial in this regard. Secondly, bibliometric coupling analysis has revealed that this field requires further expansion and in-depth study to fully understand its complexities and nuances.

The conclusion is drawn through literature research: more literature needs to be published in this field, particularly

on the coupling effect of perennial ambient temperature and environmental impact assessment (Extended Figs. 1(i; j) and Extended Table 1).

3. Methodology

The thermal load coupling effect in structural topology optimization imposes high requirements on structural strength and lightweight design to minimize component flexibility under complex boundary conditions in operation. The highly nonlinear behaviour and stress discontinuity of stress constraints under multiple loads pose new challenges for thermo-elastic analysis (Xia et al., 2018). Mathematical modeling for each element is necessary to achieve the integrated optimal performance of the thermo-elastic optimization structure model. Fig. 1 shows the entire process of the research.

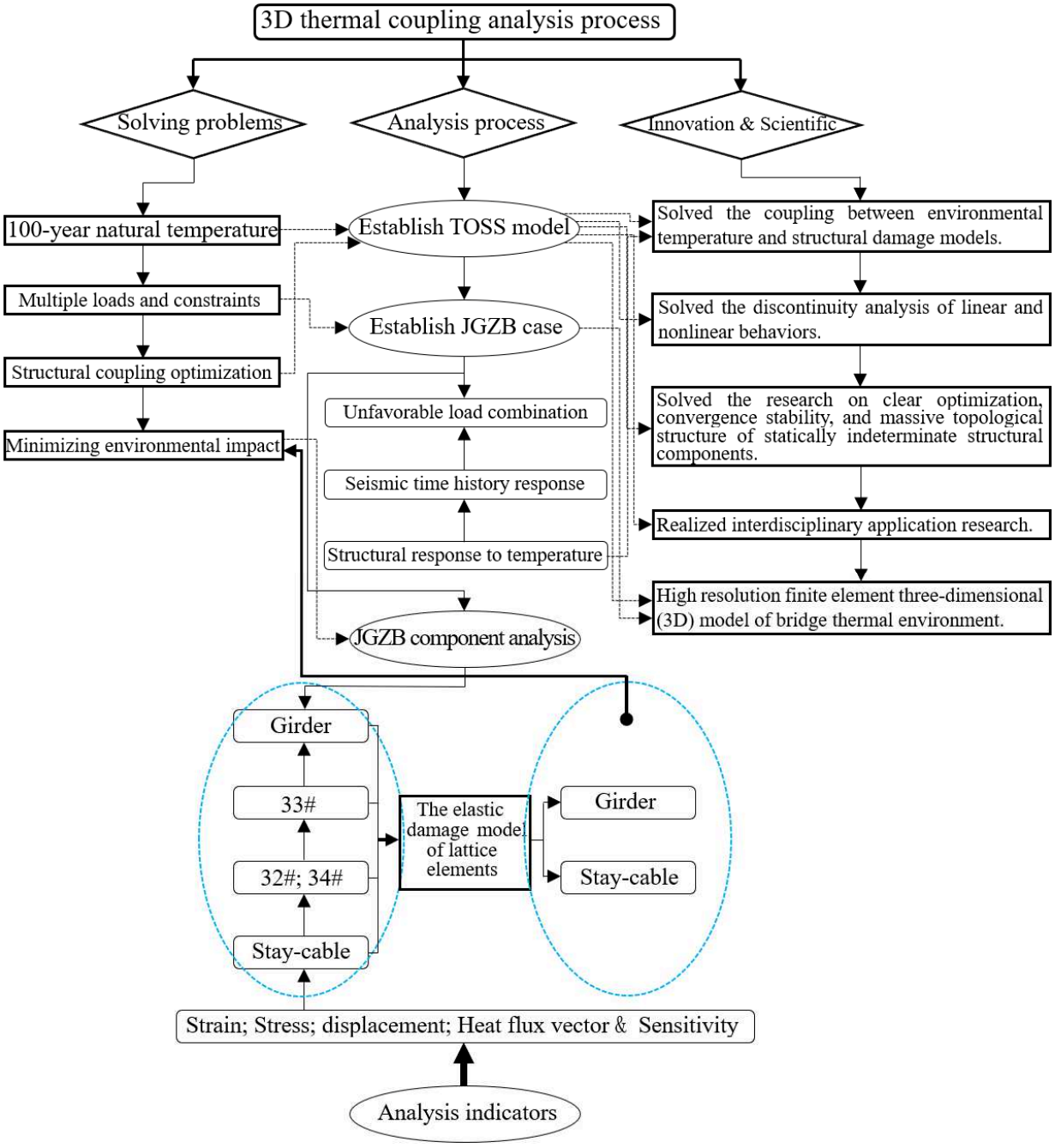

Fig. 1. The theoretical system model and analysis process flowchart of the paper.

3.1 Multi-Material Optimization Method for Thermo-Elastic Structures

Thermal-elastic finite element analysis (Wu et al., 2019; Zhou et al., 2020):

The thermal strain of the element is:

$$\delta_e^{th} = \mu_c \times \varphi \times \Delta T_e \tag{1}$$

μ_c is the thermal expansion coefficient of the material (1/degree); φ is the element vector; ΔT_e is the ambient temperature change (□).

The heat load of the element is:

$$\varepsilon_e^{th} = \int_{V_e} \Phi_e^{s-t} \times \alpha_c \times \delta_e^{th} dV \tag{2}$$

Φ_e^{s-t} is the stress and displacement matrix; α_c is the material constitutive matrix; V_e is the element volume.

The element stiffness matrix of thermo-elastic buckling material is:

$$S = \sum_{e=1}^{n} S_e^1 + \sum_{e=1}^{n} S_e^2 + \sum_{e=1}^{n} S_e^3 \tag{3}$$

n is the number of elements; S_e^1, S_e^2 and S_e^3 are the stiffness matrices of the membrane part, the bending part, and the shear part of the element, respectively. According to (1), (2), and (3):

$$S = \sum_{e=1}^{n} \int_{V_{e1}} \Phi_{e1}^{s-t} \alpha_c \mu_c \varphi \Delta T_{e1} dV + \sum_{e=2}^{n} \int_{V_{e2}} \Phi_{e2}^{s-t} \alpha_c \mu_c \varphi \Delta T_{e2} dV + \sum_{e=3}^{n} \int_{V_{e3}} \Phi_{e3}^{s-t} \alpha_c \mu_c \varphi \Delta T_e dV \tag{4}$$

ΔT_{en} is the element temperature value. The 3D structure studied in this paper is defined as[1,1,1,0,0,0] T.

3.1.1 Thermoelastic modeling of multi-material structures

$$S^T = \sum_{s_e=1}^{n} \left\{ \sum_{e=1}^{n} [s_{e1} d(s_e)] \times \lambda_{s_{e1}} + \sum_{e=2}^{n} [s_{e2} d(s_e)] \times \lambda_{s_{e2}} +, \cdots, + \sum_{e=n}^{n} [s_{en} d(s_e)] \times \lambda_{s_{en}} \right\} \tag{5}$$

S^T is the multi-material thermal-elastic stress; $\lambda_{s_{e1}}$,..., $\lambda_{s_{\mathrm{en}}}$ are the compensation factor of S_{se1} ,..., S_{sen} (In the nonlinear material constraint interval, the constraint compensation factor of the single component is considered separately, and it is the thermo-elastic coupling of the structural material under the specified boundary conditions).

3.1.2 Structure Temperature-Structure Field Coupled Optimization

The structure generates thermal stress under the action of the uneven temperature field. The thermal balance equation (Eq) is established according to the law of energy conservation:

$$\frac{\delta^2 \theta}{\delta x^2} + \frac{\delta^2 \theta}{\delta y^2} + \frac{\delta^2 \theta}{\delta z^2} = 0 \tag{6}$$

Where in, x, y and z are 3D spatial coordinates ; θ is temperature (□).

According to the linear thermal stress theory, the temperature field distribution corresponds to the change of material metric (Ozakin and Yavari, 2010). The total stress of microelements is caused by two types: the change of structural stress and the change of temperature field. The material's geometric shape and temperature deformation gradient in the study are directly related to elastic and heat stress. The thermal stress and temperature difference Eq established according to the generalized Hooke's law is expressed as:

$$\begin{cases} \varepsilon_x = \frac{[\sigma_x - \mu(\sigma_y + \sigma_z)]}{E} + \mu_c \Delta\theta \\ \varepsilon_y = \frac{[\sigma_y - \mu(\sigma_x + \sigma_z)]}{E} + \mu_c \Delta\theta \\ \varepsilon_z = \frac{[\sigma_z - \mu(\sigma_x + \sigma_y)]}{E} + \mu_c \Delta\theta \\ \gamma_{xy} = \tau_{xy}/G \,, \gamma_{xz} = \tau_{xz}/G \,, \gamma_{yz} = \tau_{yz}/G \end{cases} \tag{7}$$

Wherein: σ_x, σ_y and σ_z are the thermal stress in three directions (x, y, z) (Pa); $\Delta\theta$ is the temperature change rate (℃); G is the shear modulus of the material; τ_{xy}、τ_{yz} and τ_{xz} are the shear stress.

According to the equivalent law of shear stress (Achenbach, 2014), (6) and (7) can be transformed into:

$$\begin{cases} \tau_{xy} = \tau_{yx} = G \times \gamma_{xy} = G \times \left(\frac{\delta v}{\delta y} + \frac{\delta u}{\delta x}\right) \\ \tau_{yz} = \tau_{zy} = G \times \gamma_{yz} = G \times \left(\frac{\delta v}{\delta z} + \frac{\delta w}{\delta y}\right) \\ \tau_{xz} = \tau_{zx} = G \times \gamma_{zx} = G \times \left(\frac{\delta w}{\delta x} + \frac{\delta u}{\delta z}\right) \end{cases} \tag{8}$$

Eqs (6) to (8) represent the fundamental principles for the continuum structure's temperature-structure field coupled analysis, which are used to calculate the thermal displacement, stress, and strain. The finite element software is used to model and research the following steps: 1. analyse the temperature distribution of the structure in the temperature field using the sequential coupling method. 2. perform the structural field coupled analysis, and 3. incorporate the temperature field results into the structural field as the body load for analysis.

3.1.3 Analysis of sensitivity

The sensitivity of structural element optimization variables is the key index of structural stress research. The sensitivity modeling is completed by deriving Von Mises stress by the objective function (simultaneously considering thermo-elastic flexibility and buckling criteria).

$$\frac{\partial \delta_e^{th}}{\partial x_e} = \frac{d\delta_e^{th}(x_e)}{dx_e} \times (\mu_c \times \varphi \times \Delta T_e) \tag{9}$$

Derivation using Taylor's formula, $\frac{\partial \delta_e^{th}}{\partial x_e} = \left[\frac{d\mu^c \delta_e^{th}}{dx_e}(x_e) \times \frac{d\varphi \delta_e^{th}}{dx_e}(x_e) \times \frac{d\Delta T_e \delta_e^{th}}{dx_e}(x_e)\right]' = \frac{\partial \delta_e^{th}(\mu_c \times \varphi \times \Delta T_e)}{\partial} \times$

$$\frac{(x_e)}{x_e} + \frac{\left[\frac{\partial \cdot \delta_e^{th}(\mu_c \times \varphi \times \Delta T_e)}{\partial}\right]' \left[\frac{(x_e)}{x_e}\right]_0}{1!} \times \left\{x - \left[\frac{(x_e)}{x_e}\right]_0\right\} + \cdots + \frac{\left[\frac{\partial \cdot \delta_e^{th}(\mu_c \times \varphi \times \Delta T_e)}{\partial}\right]^n \left[\frac{(x_e)}{x_e}\right]_0}{n!} \times \left\{\left[x - \left[\frac{(x_e)}{x_e}\right]_0\right]^n\right\} \tag{10}$$

List the constant terms in Eq (7) :

$$= \frac{\partial \delta_e^{th}(\mu_c \times \varphi \times \Delta T_e)}{\partial} \times \frac{(x_e)}{x_e} + \frac{\left[\frac{\partial \cdot \delta_e^{th}(\mu_c \times \varphi \times \Delta T_e)}{\partial}\right]'}{2 \times 1} \left[\frac{(x_e)}{x_e}\right]_0 \times \left\{x - \left[\frac{(x_e)}{x_e}\right]_0\right\} + \cdots + \frac{\left[\frac{\partial \cdot \delta_e^{th}(\mu_c \times \varphi \times \Delta T_e)}{\partial}\right]^n}{n \times (n-1) \times (n-2) \times, \cdots, \times (n-m)} \left[\frac{(x_e)}{x_e}\right]_0 \times \left\{\left[x - \left[\frac{(x_e)}{x_e}\right]_0\right]^n\right\} \tag{11}$$

Optimization improve computational simplicity, it is assumed that the known terms are replaced by

$$\alpha_1, \alpha_2, \cdots, \alpha_n = \alpha_1 \times \frac{(x_e)}{x_e} + \alpha_2 \times \left[\frac{(x_e)}{x_e}\right]_0 \times \left\{x - \left[\frac{(x_e)}{x_e}\right]_0\right\} + \cdots + \alpha_n \times \left[\frac{(x_e)}{x_e}\right]_0 \times \left\{\left[x - \left[\frac{(x_e)}{x_e}\right]_0\right]^n\right\} = (\alpha_1 + \cdots + \alpha_n) \times$$

$$\left[\frac{(x_e)}{x_e}\right]' = \sum_{i=1}^{i=n} \alpha_n \left[\frac{(x_e)}{x_e}\right]' \tag{12}$$

$\alpha_n = \frac{\left[\frac{\partial \cdot \delta_e^{th}(\mu_c \times \varphi \times \Delta T_e)}{\partial}\right]^n}{n \times (n-1) \times (n-2) \times, \cdots, \times (n-m)}$, μ_c is the thermal expansion coefficient of the material; φ is the element vector; ΔT_e is the ambient temperature change (℃); δ_e^{th} is the strain energy of the structure.

The conclusion is that several factors influence the sensitivity of topological optimization for multiphase materials under non-uniform temperature fields. These factors include the material's heat flux matrix, the unit body's stiffness matrix, the node's heat conduction matrix, and the temperature change rate vector.

3.2 Analysis of environment

Our previous research on the sustainable development of cable-stayed bridges involved establishing a multi-factor decision-making model, which was used to assess the contribution of environmental impact across five stages in the

published literature (Zhou et al., 2020). It should be noted that this manuscript is intended for reference purposes only.

$$E_T = \begin{cases} E_D = \sum_{T_s=Investigation}^{T_f=Contract} E_{D_N} \{[(M_{D_1} \times \mu_{D_{E1}}) \times (1 \pm l_{D_{\lambda 1}})] + \cdots + [(M_{D_n} \times \mu_{D_{En}}) \times (1 \pm l_{D_{\lambda n}})]\} \\ E_M = \sum_{T_s=Prepare}^{T_f=End} E_{M_N} \{[(M_{M_1} \times \mu_{M_{E1}}) \times (1 \pm l_{M_{\lambda 1}})] + \cdots + [(M_{M_n} \times \mu_{M_{En}}) \times (1 \pm l_{M_{\lambda n}})]\} \\ E_C = \sum_{T_s=Start}^{T_f=Operation} E_N \{[(M_{C_1} \times \mu_{C_{E1}}) \times (1 \pm l_{C_{\lambda 1}})] + \cdots + [(M_{C_n} \times \mu_{C_{En}}) \times (1 \pm l_{C_{\lambda n}})]\} \\ E_S = \sum_{T_s=Use}^{T_f=During} E_N \{[(M_{S_1} \times \mu_{S_{E1}}) \times (1 \pm l_{S_{\lambda 1}})] + \cdots + [(M_{S_n} \times \mu_{S_{En}}) \times (1 \pm l_{S_{\lambda n}})]\} \\ E_O = \sum_{T_s=Demolition}^{T_f=Cleaned} E_N \{[(M_{O_1} \times \mu_{O_{E1}}) \times (1 \pm l_{O_{\lambda 1}})] + \cdots + [(M_{O_n} \times \mu_{O_{En}}) \times (1 \pm l_{O_{\lambda n}})]\} \end{cases} \quad (13)$$

E_T is environmental impact contribution data (kg, from project planning to demolition and cleaning); E_D; E_M; E_C; E_S; E_O are environmental impact data during design, materials, construction, maintenance and demolition (kg); M_{D_1}; M_{M_1}; M_{C_1}; M_{S_1}; M_{O_1} are loss data in five stages (kg); $\mu_{D_{E1}}; \mu_{M_{E1}}; \mu_{C_{E1}}; \mu_{S_{E1}}; \mu_{O_{E1}}$ are emission coefficient corresponding to energy consumption (kg/kg); $l_{D_{\lambda n}}; l_{M_{\lambda n}}; l_{C_{\lambda n}}; l_{S_{\lambda n}}; l_{O_{\lambda n}}$ are loss coefficient of energy consumption (%).

The life cycle inventory for environmental impact comprises ten core indexes based on the ISO 14040:2006 framework and the CML 2001 standard. Two methods, midpoint, and endpoint, are used for LCA feature modeling. Midpoint analysis is used for process analysis, and endpoint analysis is used for the regional representation model. Monte-Carlo Simulation is employed in the Open LCA software system model to account for uncertainty factors. During data entry, the weight of influence is adjusted based on quantitative experience. The research focuses on a variable cross-section structure for the bridge, with the functional element defined as a 1 kg effective weight.

3.3 Fixing theory of lattice porous mechanics

To analyze the fracture and propagation of porous and brittle materials, modeling the structural crack coupling is crucial in predicting fluid pressure and structural failure. The coupled transmission and mechanical lattice model simulates porous materials' fracture. At the same time, the discrete process analysis is used to investigate the fracture and propagation of brittle materials. P. Grassl (Pham et al., 2021) has recently proposed the coupled lattice fluid mechanics method to analyze the coupling effect of elastic half-crack and driving crack.

The elastic damage model is used to respond to the lattice element, and the law is:

$$\alpha^m = (1 - \delta) \times \theta \times \varepsilon \quad (14)$$

α^m is the stress vector; ε is the strain vector (normal strain, shear strain and rotational strain); δ is the damage parameter; θ is the elastic stiffness (Griffiths and Mustoe, 2001).

$$\begin{cases} \theta = \begin{bmatrix} E & 0 & 0 \\ 0 & \lambda E & 0 \\ 0 & 0 & E \end{bmatrix} \\ \lambda = \frac{1-3\nu}{\nu+1} \\ E = \frac{E_c}{1-\nu} \end{cases} \quad (15)$$

E and λ are regular lattice and plane stress analysis parameters of the equilateral triangle; E_c is young's modulus of the continuum; ν is the Poisson's ratio.

4. Results and discussion

The Jian Ma Bridge (JGZB) is a cable-stayed bridge spanning a river on the San Shui Expressway in China. With

a total length of 566m and a vehicle speed of 120km/h, the bridge is designed to accommodate the load standard of an extra 20 and trailer-120 vehicles. The bridge features a double cable plane and a single tower, supported by a T-shaped rigid frame that forms a cooperative system. The span combination of 60 m + 223 m + 223 m + 60 m. The cable distance on the beam is 8 m, which is reduced to 4 m in block 26#. The bridge has 56 pairs of cables. The T-frame girder is a twin box single-cell section with a width of 26.5 m and a height ranging from 2.11m to 7.90m. The primary and side piers of the rigid frame are double thin-walled flexible piers.

The towers, piers, and beams of the cable-stayed bridge are solidified. The girder has a Π-shaped section with a width of 28.6m and a height of 2 m. A standard construction section has a length of 8 m, with 27 sections on each side. The 0# block is 12.2 m long, the 1#~25# blocks are 8 m long, and the 26# block is 6.8 m long and is a closure section. The 27# block is also a closure section with a length of 1.42 m. Each girder section has two diaphragms spaced 4 m apart. The web is 2 m high and 28 cm thick. Fig. 2 shows the box section bridge tower and pile foundation under the bearing platform.

The central tower has a portal cable tower design with a high pile cap (with dimensions of 37.50 m×22.50 m×6.15 m ($C30$)). The foundation has 24 bored piles with a variable section of 2.50~2.85 m. The upper tower column has a box section measuring 3 m×8 m with a wall thickness of 0.65 m and 1.20 m ($C50$). The middle tower column has a 3 m×8 m box section with a wall thickness of 0.8 m and 0.9 m ($C50$). The lower tower column has a 5.0 m×10.4 m~5.0 m×8.0 m box section with a wall thickness of 0.9 m ($C40$).

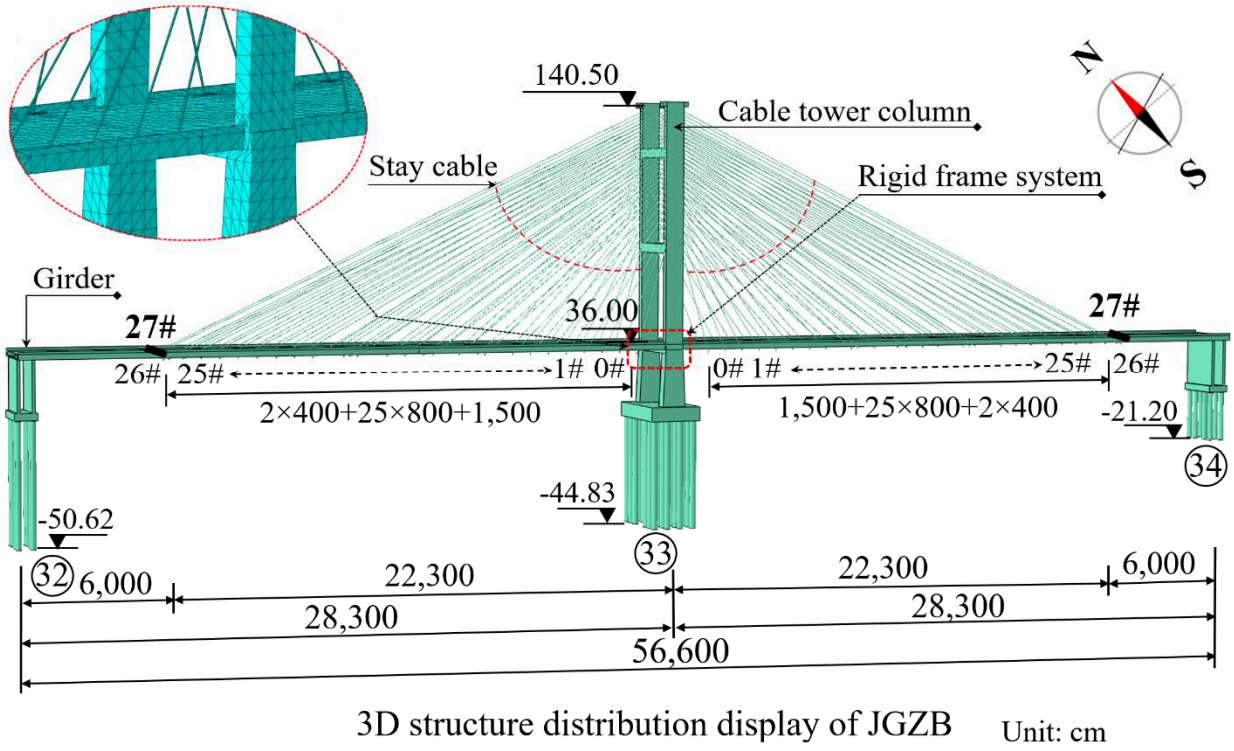

Fig. 2. 3D solid facade model of JGZB.

4.1 Analysis of load

JGZB, which was constructed in 1999, was designed five years prior in 1994 and was built under the design regulations outlined in the China highway bridge construction standards (JTJ (construction standards for the transportation industry) 001-97; JTJ021-89; JTJ023-85; JTJ024-85; JTJ027-96; JTJ004-89) (Lian et al., 2021). The bridge is situated in a subtropical region with an average annual temperature of 21.9℃ and experiences extreme temperatures ranging from a maximum of 39.1℃ to a minimum of 0.7℃. Additionally, the bridge was designed to withstand a seismic intensity of 7° and to resist an essential wind pressure of 700Pa (Huang et al., 2006).

The finite element coupled analysis was performed using the limit state method without considering multiple accidental action combinations. Once the standard value was calculated, a specific partial action coefficient was applied to account for the most unfavourable combination effect in the coupled analysis, as outlined by Liu et al., (2016). Table 1 shows the load data obtained from the analysis.

Table 1

Design data of the most unfavourable load combination of JGZB.

Load name		Number (N/m²)
Permanent effect	Water buoyancy	4,026.66
	Vehicle load	6.81
Variable effect	Vehicle impact	34,330
	Vehicle centrifugal force	15,448.5
	Vehicle braking force	The line is a straight line
	Crowd load	4,200
	Fatigue load	3,150
	Temperature load	See 4.1.2
	Wind load	142,345.90 N/m (Pile foundation); 89,902.72 N/m (Pier coping); 37,084.87N/m (Pier column); 1,487,328.12N/m (Pylon)
Accidental effect	Bearing friction	0.3w (w= Gravity above the bearing pad stone)
Earthquake effect	JTG/T B02	See 4.1.1

Notes: The new standard code JTG D60-2015 is used for the design load analysis, which mainly assesses the data in the operation stage.

4.1.1 Seismic time history response analysis

JGZB is a super central bridge with a single span more significant than 150m, and its seismic fortification intensity is classified as Class A. Based on the seismic action of E1, which represents ground motion parameters with a 50-year exceedance probability and 72-year recurrence interval, the structure is not expected to suffer damage within the elastic range, and both the structural strength and stiffness are expected to remain unchanged. For seismic resistance calculations, the entire section stiffness of the bridge was adopted, as Zu et al., (2022) noted. The researchers also found that ground motion exhibits complex spatial variation characteristics, including coherence, traveling wave, and local site effects that can significantly affect the seismic analysis of long-span bridges. To address these effects, seismic analysis using multi-point non-uniform excitation was found to be more robust, according to Wen et al., (2022).

Wang et al., (2015) proposes a precise step-by-step integration method to calculate the dynamic structural response, and the integration format is shown as follows:

$$V_{(tk+1)} = T(\tau) \times \left[V_{(t_k)} + H^{-1}{}_{r_0} + H^{-1}{}_{r_1}\right] - H^{-1}{}_{r_0} + H^{-1}{}_{r_1} + r_1 + r_1 \times \tau \quad (16)$$

$V_{(tk+1)}$ is the solution of the Eq; $T(\tau)$ is a matrix; r_0 and r_1 are invariant vectors; t is the step of each integration; τ is t-t_k.

JGZB was analyzed using Eq (15), and the damping ratio is 0.05. The analysis considered the coupling effect of the axial force, the main cable's sag, and the girder's bending moment. The longitudinal displacement of the vibration component at the connection between the girder and T-frame was 6.24 cm. The longitudinal displacement at the top of the central tower was 5.08 cm. Based on the internal force time history analysis, the maximum bending moment at the consolidation of the central tower, girder, and pier was determined to be 5.246×10^3kN·M. The vibrations of the girder, central tower, and T-frame mainly caused the transverse vibration component of the bridge, with the maximum bending moment calculated to be 2.775×10^3kN·M.

4.1.2 Structural response due to temperature effects

The temperature effect was analyzed based on the design specification data (He et al., 2021). The JGZB structure is primarily reinforced concrete and steel, with linear expansion coefficients of 0.000010/ºC and 0.000012/ºC, respectively. Since the bridge is in a warm region, the external or constrained deformation caused by temperature must consider the maximum and minimum effective temperatures. The design code recommends using 39ºC as the highest and 0ºC as the lowest temperature values. To facilitate thermal stress research and analysis during maintenance, a study was conducted on the solar orbit over San Shui City, China. The angle between JGZB and the equator was calculated to be 12.407º. Fig. 3 displays the relevant data, which provides valuable insights into the bridge's thermal behaviour.

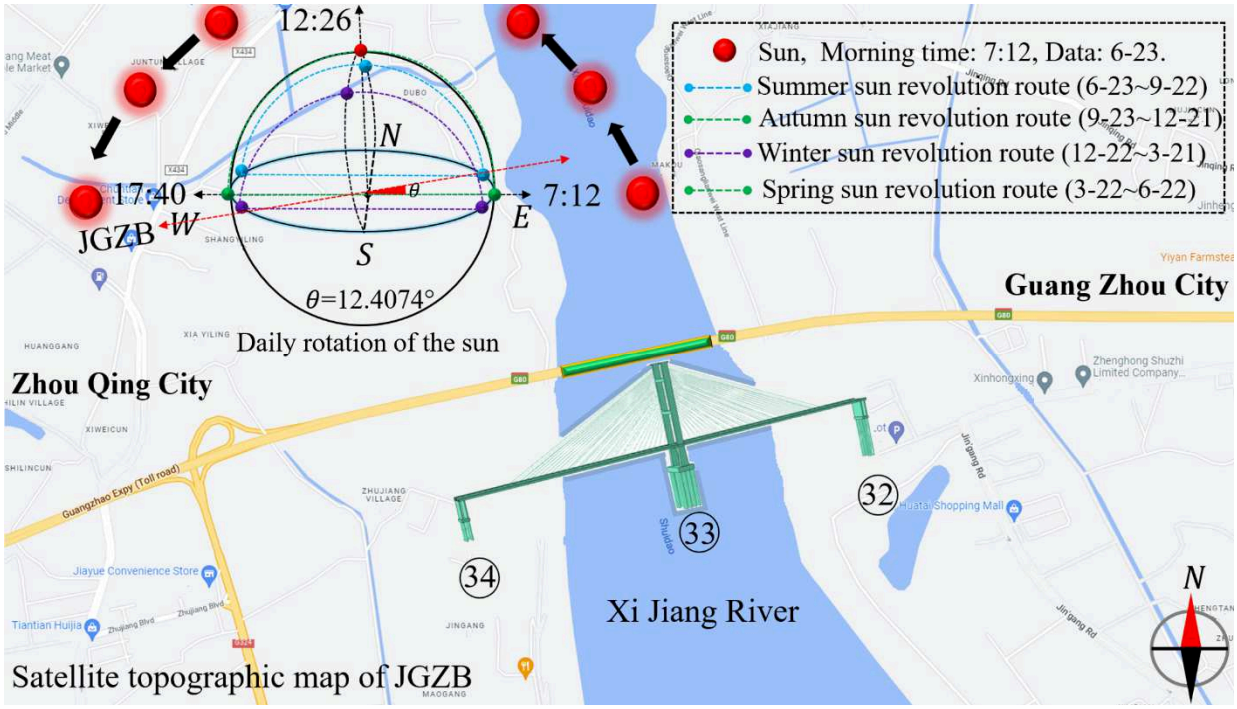

Fig. 3. JGZB 's daily and yearly solar orbit photos (trajectories of China).

4.2 Finite element thermoelastic analysis under standard design environment

The finite element mesh division for JGZB was daunting due to the bridge's sizeable span-to-height ratio of 3.05:1. There are five parts to divide the mesh. The whole JGZB is divided into 350,109 groups of meshes, and that of analysis warning is 66,004 groups, accounting for 18.85% of the total.

The thermal stress coupled analysis followed the design specifications, considering the bridge's concrete composition, reinforcement, and Φj15.24 stainless steel strand. Table 2 shows the various parameter settings used in the analysis. The analysis was conducted using Abaqus software in five steps, with a total time of 1 minute.

Table 2

Thermal stress coupled finite element setting parameter data of JGZB.

Parameter	Unit	Concrete	Asphalt	Air	Steel
Thermal conductivity	w/(m·□)	1.54	2.45	0.025	56
Mass density	kg/m³	2,270	2,110	0.001,3	7,800
Young's modulus	pa	32,300,000,000.0	1,200,000,000.0	/	195,000,000,000.0
Poisson's ratio	/	0.249	0.256	/	0.255
Expansion Coeff alpha	1/□	0.000,009,0	0.000,007,5	0.000,001,25	0.000,012,2

Heat capacity	J/kg·□	955	960	1.006	460

Fig. 4 shows the finite element thermal coupling analysis image of JGZB. The temperature and displacement gradients of the girder component are prominently displayed. The temperature and displacement gradient of the girder in the component are robust. 32#~33# are divided into twelve temperature and displacement gradients, symmetrically distributed on both sides of area 1 (between 18# and 23# steel strands). 33#~34# are divided into ten temperature and displacement gradient groups distributed on both sides of area 1 (between 21# and 23# steel strands). The 3D solid research captures the structural and thermal coupling details of JGZB, providing an innovative and scientific approach to this analysis (see Fig. 4).

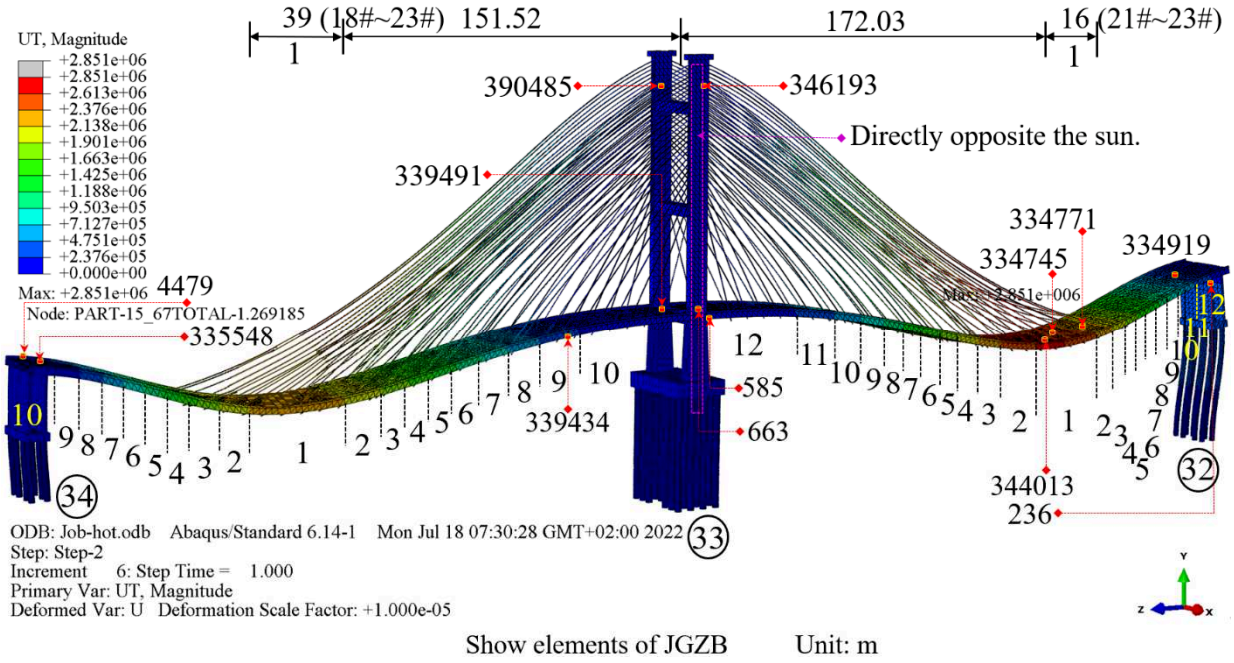

Fig. 4. Total displacement vector finite element coupled model (cartesian coordinate system).

4.2.1 Analysis of girder

The girder of JGZB is subjected to coupled thermo-mechanical analysis and monitored using 65 monitoring points located in the top plate area. The displacement and stress distributions are presented based on the observations of these points. The top five groups of displacement, namely 344013, 334745, 339036, 5519, and 5627, are all located in Area 1. In comparison, the top five stress groups, namely 334771, 334745, 4479, 335548, and 334919, are concentrated in area 2, as shown in Fig. 4. Interestingly, the distribution areas of displacement and temperature gradient are found to be the same. It is worth noting that the maximum stress points are located above the 32# and 34# supports, indicating the need to check the stress concentration and damage of the primary pier support during maintenance (Rahmzadeh et al., 2021).

The heat flux vector (HFL) is a critical parameter used to monitor the amount of heat energy per unit area. It accurately quantifies and characterizes a material's thermal conductivity and thermal resistance. The first five HFL and strain parameters from the 65 monitoring points are as follows: 339491, 344013, 4469, 5627, and 4422. These monitoring points are located at the consolidation of the girder, tower, and pier, the area with the highest heat flow density of the entire bridge. The research data verify the robustness of the Chinese code JTG/T 3365-01-2020, which indicates that the tower beam pier consolidation system has significant overall stiffness and large temperature internal force. The design system suits cable-stayed bridges with high piers and appropriate flexibility. Monitoring point 344013 is located in area 1 of 32#~33#, and the thermal displacement is also concentrated in this area. The data from the other three groups of monitoring points are all low, as shown in Figs. 4 and 5(a). The ranking of strain

monitoring points is as follows: 334771, 334745, 4479, 344013, and 338133. The most significant data monitoring points are concentrated in areas 1 and 2 of 32#~33#. The analysis conclusion is consistent with stress, as shown in Figs. 4 and 5(b).

There are 70 monitoring points on the bottom plate of the girder. The first five stress groups are 236, 237, 5054, 339345, and 574. After comparing the data, it was found that the stress on the bottom plate is 1.704 times higher than that on the top plate (236~334771 monitoring points), with the maximum stress located at the connection between the 32# main pier and the girder's bottom plate (Fig. 4). The other four groups of monitoring points are located in area 1 of 32#, 34#, and 33#~34#. The stress data are consistent with those of the top plate (Fig. 5(c)). The first five displacement groups are 343433, 343678, 5916, 344035, and 343984. These five monitoring points are all in area 1 of 32#~33#, consistent with the distribution of roof displacement and temperature displacement areas (Figs. 4; 5(c)). The same monitoring points were selected for measuring the strain and HFL of the girder's bottom plate. The first five strain groups are 236, 334314, 574, 6197, and 343936, with the positions of monitoring points consistent with those of stress. The ranking of HFL is 339434, 343678, 339345, 339549, and 343689, with the positions of monitoring points consistent with those of the top plate.

The first monitoring point is still in area 9 of 33#~34#, indicating that the energy is gradually diffused and decreased during the transmission of temperature stress (Figs. 4; 5(d)).

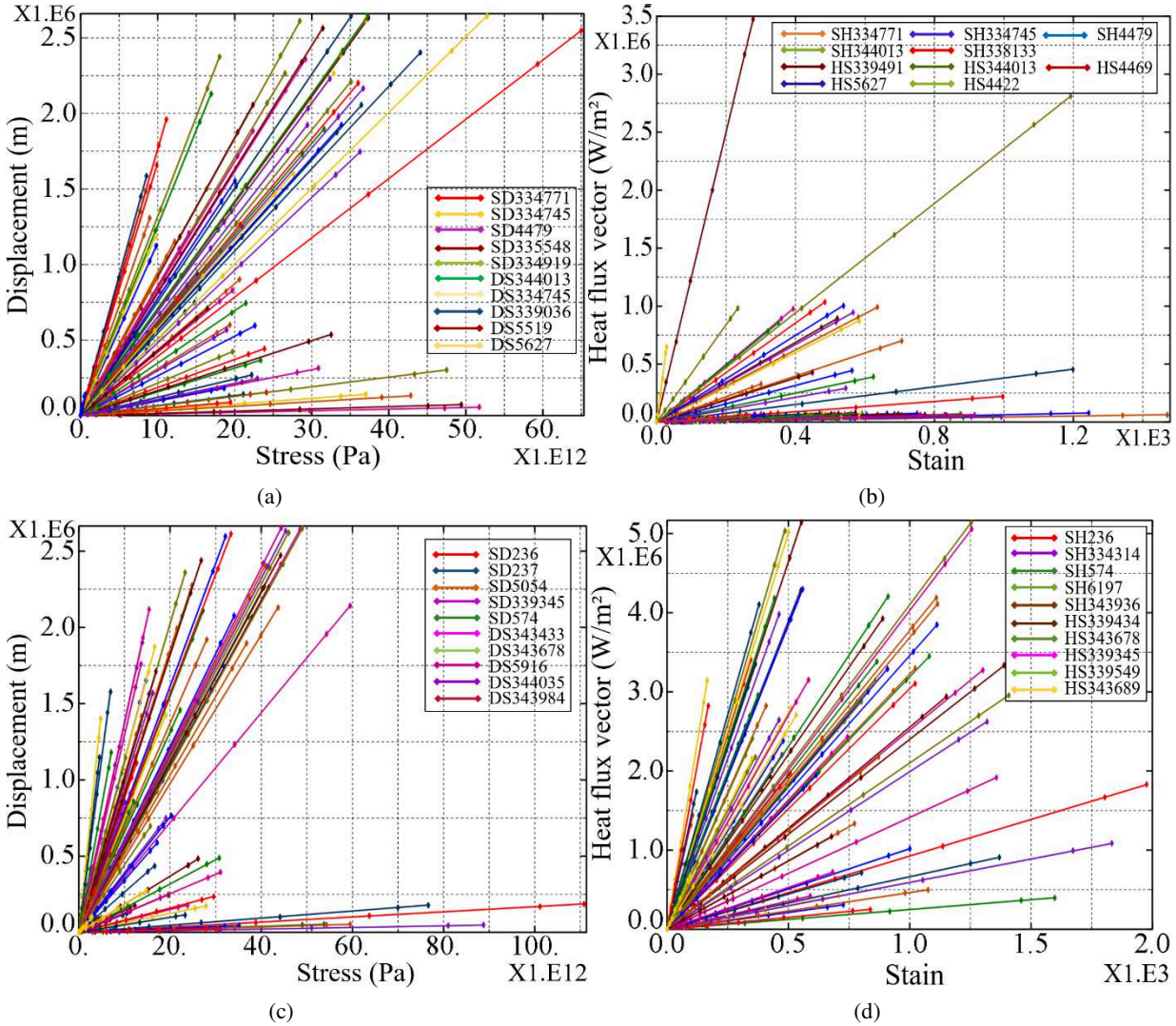

Fig. 5. Thermal coupling design analysis (girder). (a) Stress- Displacement (top plate); (b) Stain- HFL (top plate); (c) Stress- Displacement (bottom plate); (d) Stain- HFL (bottom plate).

4.2.2 Analysis of 33#

Ninety monitoring points are installed on the 33# central tower, the main area of thermal stress in the JGZB. The first five stress groups are ranked as 346193 > 390485 > 585 > 663 > 347413, and the two groups with the highest stress are located at the intersection of the fourth stay cable and the central tower, specifically at positions 346193 and 390485 on the tower's top (see Figs. 4; 6(a)). The thermal stress effect causes stress to concentrate at the top of the tower. Regarding displacement, the first five groups are 948 > 390531 > 348492 > 863 > 348613, all concentrated at the top of the central tower. The thermal stress induces significant displacement at the tower's top. Based on the temperature gradient data, stress is concentrated on the opposite solar radiation side of the central tower (see Figs. 3, 5; 6(a)).

The first five groups of strains at 33# are as follows: 585, 663, 1658, 357416, and 8824. The two groups with the highest strain monitoring points, 585 to 663, are concentrated at the consolidation of the girder, central tower, and pier, as shown in Fig. 9. In contrast, the other groups are scattered at the top of the tower and pile foundation, as seen in Fig. 6(b). Regarding HFL, the top five groups are 8824, 1658, 1848, 663, and 347413. The front of the central tower, marked by the purple box in Fig. 4, is directly exposed to the sun. It represents the heat energy concentrated flow area with the strongest density field, as depicted in Fig. 6(b).

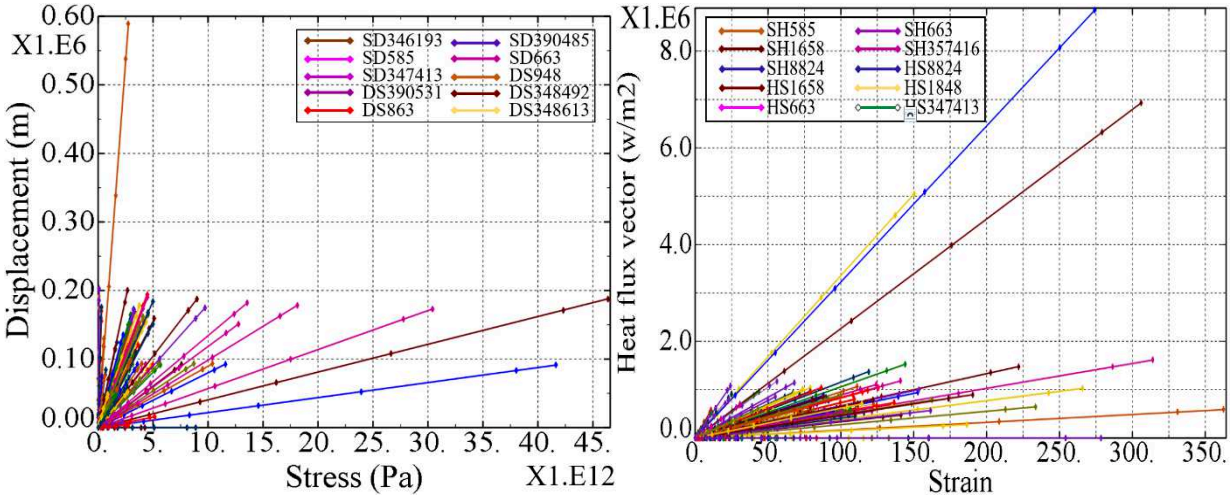

(a) (b)

Fig. 6. Thermal coupling design analysis (33#). (a) Stress- Displacement; (b) Stain- HFL.

4.2.3 Analysis of 32# and 34#

There are 45 monitoring points for the 32# and 34# piers, including the pile foundation, bearing platform, pier column, and pier cap.

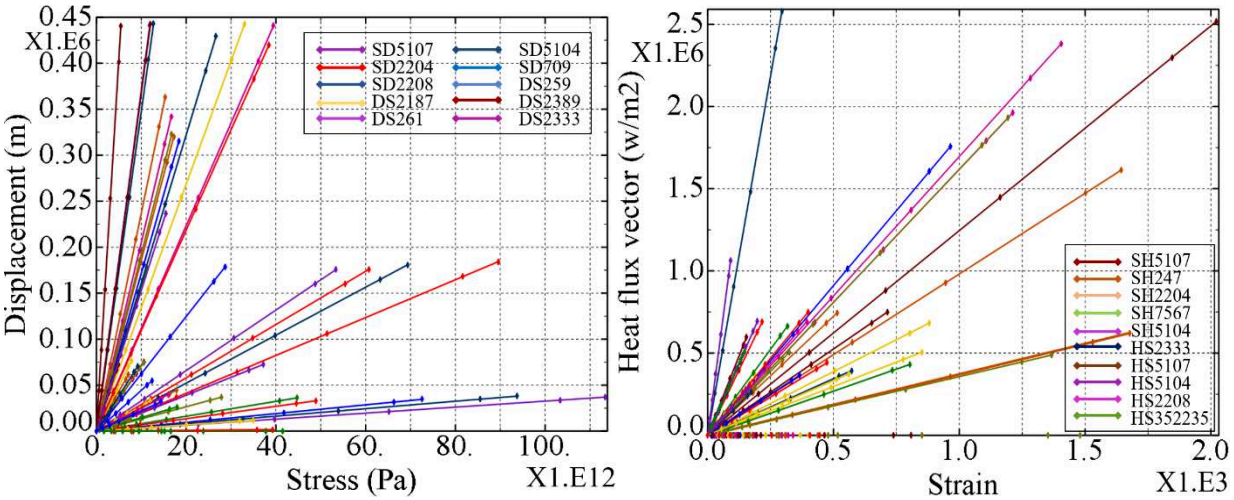

(a) (b)

Fig. 7. Thermal coupling design analysis (32#,34#). (a) Stress- Displacement; (b) Stain- HFL.

The first five stress groups are 5107, 5104, 2204, 709, and 2208, with the maximum stress concentration area at the connection between the 33# bearing and girder, as shown in Fig. 7(a). As for displacement, the first five groups are 259, 2187, 2389, 261, and 2333, with the maximum displacement concentrated at the capping beam of the 32# pier. Currently, the heat energy in areas 1 and 2 of the 32#~33# girder is rapidly transferred to the 32# pier through heat transfer, causing a significant reduction in the thermal displacement vector. The maximum displacement of the 32# pier is only 16.73% of that of the girder, as depicted in Fig. 7(a).

The first five groups of strain are as follows: 5107, 247, 2204, 7567, and 5104, with the maximum strain located at the connection of the 34# pier and girder, as shown in Fig. 7(b). Regarding HFL (w/m^2), the first five groups are 2333, 5107, 5104, 2208, and 352235. The maximum heat flux density is at the 32# pier, consistent with the conclusion drawn from the thermal displacement analysis, as depicted in Fig. 7(b).

4.2.4 Analysis of stay-cable#

The stay cable is a critical component of JGZB as it is a thermal stress concentration point. The deformation caused by ambient temperature's thermal stress can lead to coupling changes in the bridge structure. Due to the highly nonlinear effects of the structural components, the static and dynamic responses of cable flexibility and mechanical damping can gradually deteriorate, making the stay cable a focal point of research (Montassar et al., 2015). There are 152 monitoring points for the stay cable, with the first ten stress groups being 259541, 256907, 164793, 176351, 175355, 174622, 161702, 162652, 161932, and 264670.

Analysis data and location show that the maximum thermal stress is concentrated at the top of the central tower. The distribution ratio of thermal stress monitoring points of 32#~33#:33#~34# is 5:4, with the stress concentrated at the upper steel strand of areas 1 and 2, respectively, as illustrated in Figs. 8(a), (c).

According to the analysis, the top ten displacement groups are 264670, 273472, 175355, 192926, 273099, 307392, 315531, 269758, 226637, and 219347, as shown in Fig. 8(a). The displacement is concentrated above area 1 of 32#~33#, illustrated in Fig. 4. The ranking of the strain is 162652, 256907, 176351, 161932, 266380, 161702, 28579, 269758, 274402, and 14560. The thermal strain monitoring points are distributed in 32#~33# and 33#34#, accounting for 50% each. The strain is concentrated above area 37, as depicted in Fig. 8(b). The heat flux vector (w/m2) ranking is 187740, 17325, 179135, 259541, 174622, 263686, 21463, 277012, 164793, and 151444. Seven groups of heat flux density are concentrated at the top of the tower; two are located in area 2 of 32#~33#, and the others are distributed in area 3 of 33#~34#, as shown in Fig. 8(b). The thermal stress resulting from the temperature has the most significant coupling effect on the central tower.

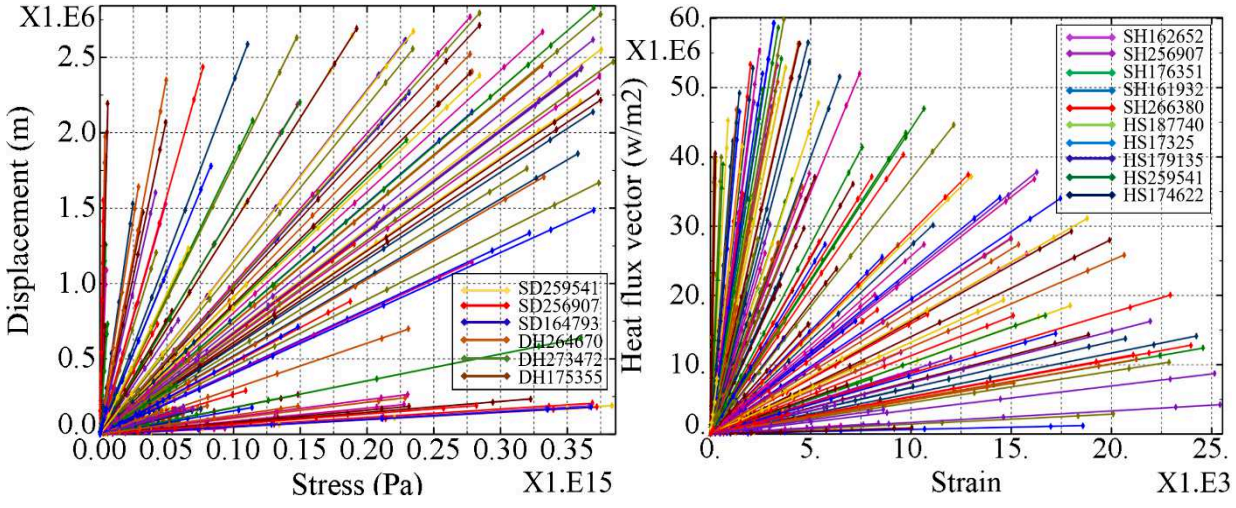

(a) (b)

Fig. 8. Thermal coupling design analysis (stay cable). (a) Stress- Displacement; (b) Strain- HFL.

4.2.5 Analysis of sensitivity

In section 3.1.3, a mathematical model is developed to examine the thermal stress coupling sensitivity of JGZB. Its components' sensitivity change data are analyzed within the design temperature range (0℃ < T < 39℃) to serve as the benchmark for optimization in section 4.3.

α_x correlates μ_c, φ, ΔT_e and δ_e^{th}. The first three of the four variables are the determined values, and δ_e^{th} is the variable. Four groups of parameters in temperature thermal coupling determine δ_e^{th}: $\sigma_{x,y,z}$ (stress), Φ_e^{s-t} (displacement), δ_e^t (strain) and S^T (3.1.1;3.1.2). Ten groups of monitoring points (the first ten groups) are selected to analyse the sensitivity range.

$\alpha_{\text{Girder top}}$ = 6.06×10^{28}~8.80×10^{29}; $\alpha_{\text{Girder bottom}}$ = 2.16×10^{28}~3.13×10^{30}; $\alpha_{33\#}$ = 3.03×10^{25}~1.98×10^{28}; $\alpha_{32\#\sim34\#}$ = 7.50×10^{27}~1.75×10^{29}; $\alpha_{\text{Stay cable}}$ = 1.10×10^{33}~1.65×10^{33}.

4.3 Finite element thermoelastic analysis in natural environment

JGZB commenced operation in 2000. We developed a thermal-solid coupling model for uneven temperature fields in Section 3.1.2. We obtained the coupling data for an ambient temperature of multiphase materials under the design boundary conditions in Section 4.2. The critical question is whether the design meets the optimal performance indices. In Section 4.3, we determine the optimal design. Scientific research using meteorological satellites reveals that global surface temperatures have steadily increased, particularly in the past decade (Derdouri et al., 2021). For the research time interval, we selected the meteorological data from the area where the bridge was located between 2011 and 2021 as the optimal boundary condition for the temperature field (data source: National Meteorological Information Centre (Yao et al., 2022)).

Based on the statistics of the maximum and minimum temperatures from 132 months (2011-2021) (Fig. 9(a)), a normalization analysis was conducted to determine the temperature boundary for thermal stress coupled analysis of JGZB. The analysis revealed that high temperatures were predominant, with the highest temperature recorded in 2020 (Fig. 9(b)). Consequently, the temperature range of 1℃ to 38℃ was selected as the temperature boundary for the thermal stress coupled analysis of JGZB.

In the coupled optimization of temperature thermal stress of JGZB, 328 monitoring points are monitored, divided into four parts: girder, 33#, 32#~34#, and stay-cable. Each part's first ten monitoring points are selected for analysis and research.

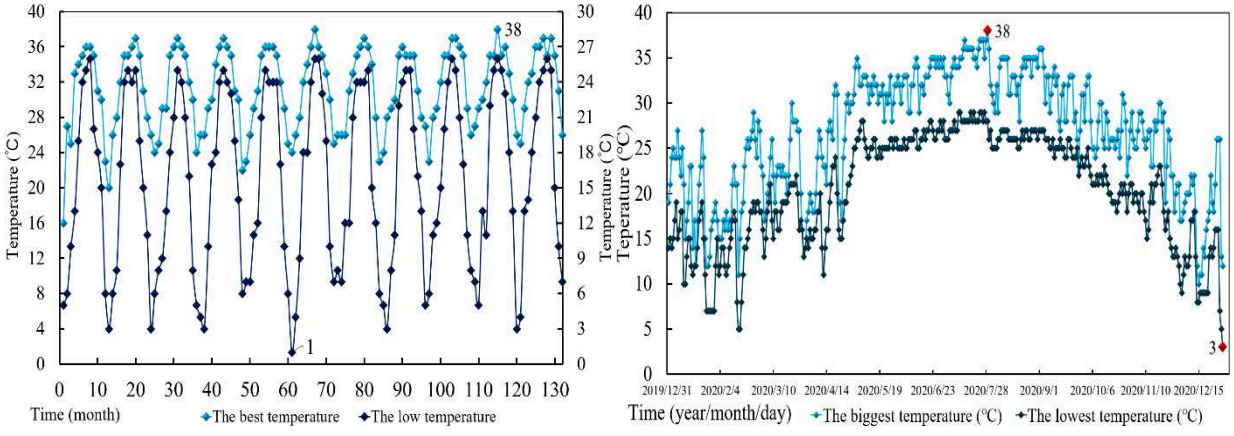

(a) (b)

Fig. 9. Monthly temperature data from 2011 to 2021. (a) Time- temperature; (b) Temperature of 2020.

4.3.1 Analysis of girder (interval of new time)

Based on the newly established temperature thermal stress model, component indices were analyzed according to Section 3.1.2. The data of 62 groups of monitoring points selected for the girder are presented below:

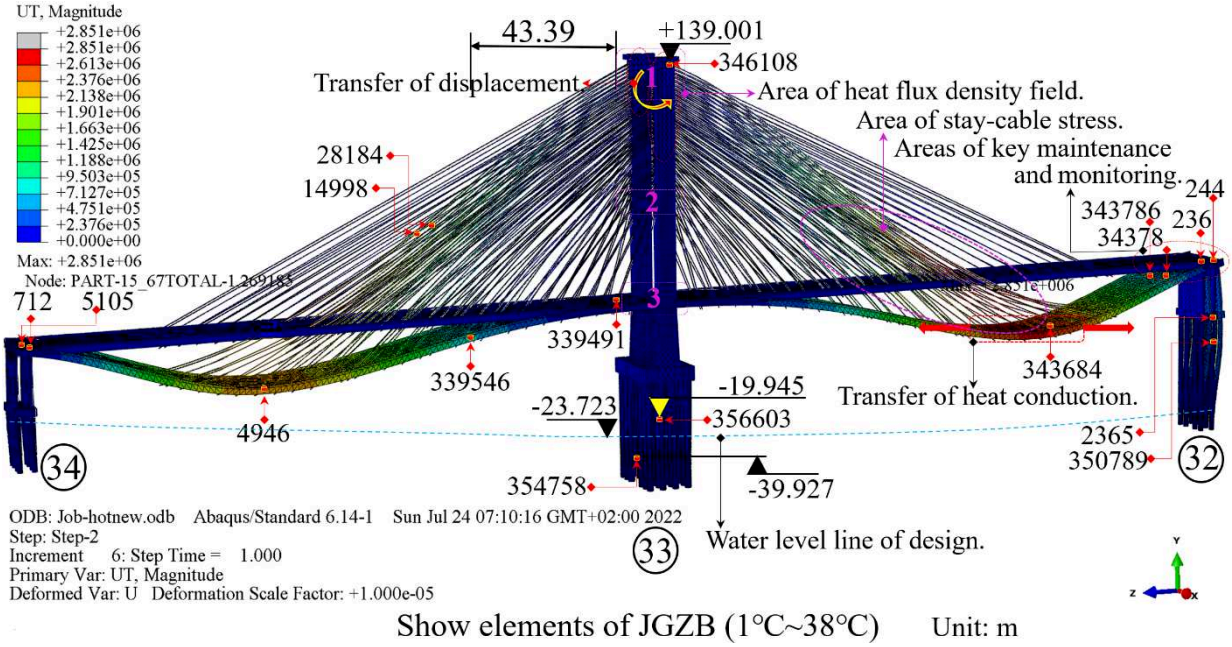

Fig. 10. Focus on the vector finite element coupled model (cartesian coordinate system).

Stress: The stress values for 62 monitoring points are shown in Figs. 11(a), (c), with the top 10 groups being 712, 236, 343783, 5105, 343786, 244, 343684, 5919, 5053, and 4946. Four monitoring points (236, 244, 343793, and 343786) are located on the girder above 32#, while three monitoring points (712, 5053, and 5105) are above 34#. The high-temperature thermal stress (the first three groups) is concentrated on the girder above 32# due to heat conduction from area 1 of the original 32#~33# to the girder of 32# and 34#.

Displacement: The top 10 groups of displacement values for the 62 monitoring points are shown in Figs. 11(a), (c), with 343990, 341436, 5919, 342274, 343443, 339222, 4946, 5046, 339152, and 339313 is the highest values. The variation between displacement and temperature does not affect the maximum displacement position.

Strain: The top 10 groups of strain values for the 62 monitoring points are shown in Figs. 11(b), (d), with 343783, 712, 236, 5105, 343786, 244, 343990, 5919, 339213, and 344276 being the highest values. There are four groups of high-strain points (343783, 236, 343786, and 244) on the girder above 32#, of which three groups (343783, 244, and 343786) are two-component points (with high stress and high strain). Therefore, it is determined that 32# is the critical structure for JGZB to maintain and monitor.

The HFL data for JGZB components are as follows: 339546 > 343684 > 339454 > 339818 > 343467 > 343443 > 343474 > 339152 > 343734 > 333471 (Figs.11(b), (d)). Note that 339546, resulting in a 43.39 m shift in position

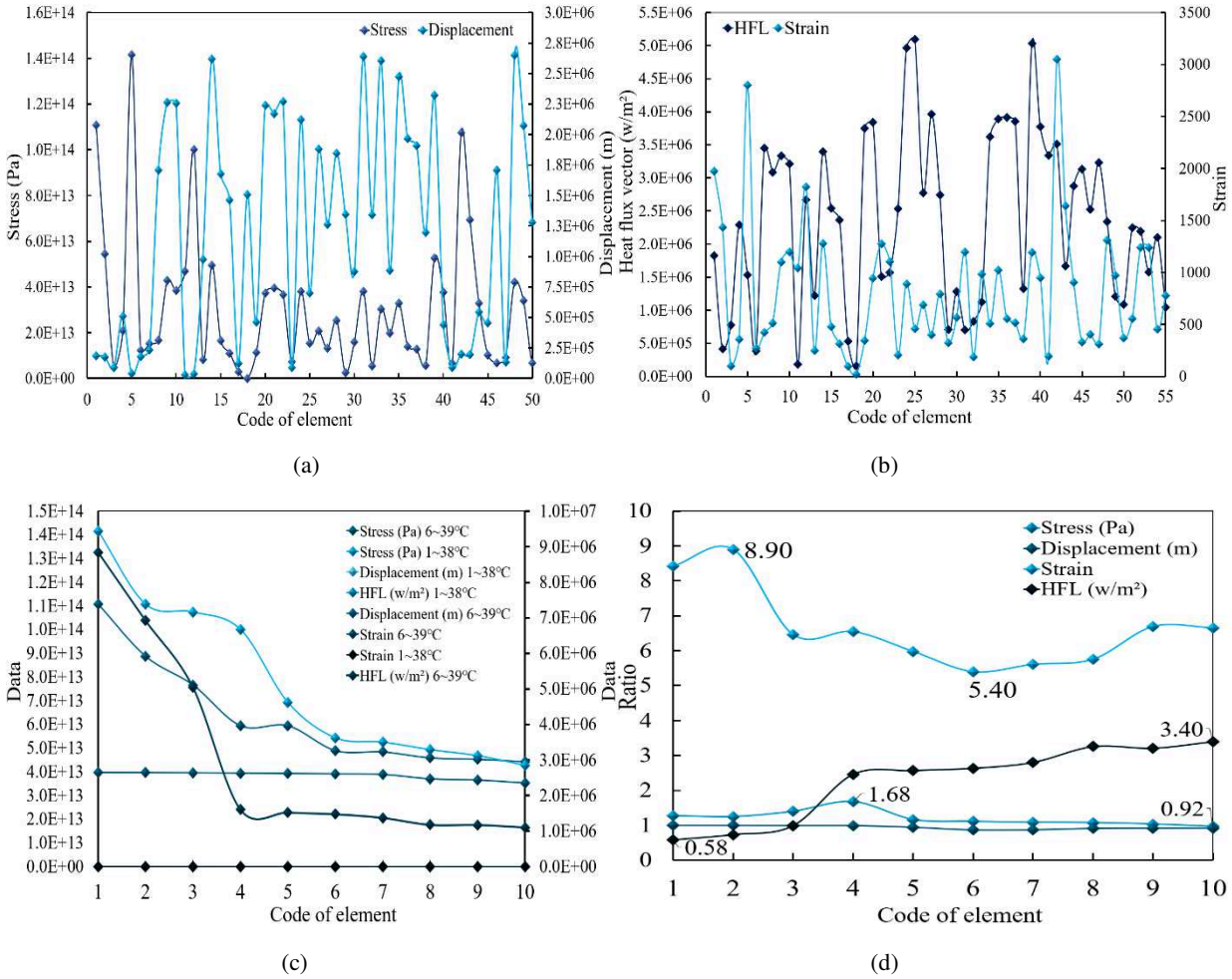

Fig. 11. Thermal coupling design analysis. (a) Data comparison of S-D (bottom plate); (b) Data comparison of S-H (bottom plate); (c) Comparison of thermomechanical coupling data at two temperatures; (d) Ratio of elements.

from 33# to 34# (Fig. 10), we have replaced the highest monitoring point identified initially as 339491. This indicates that changes in ambient temperature result in a dynamic flow effect of heat flux at each girder interface. These findings suggest that the temperature thermal stress-coupling model has a simulation and equivalent relationship with fluid dynamic theory (Balbay and Esen, 2013).

Compared with the thermal coupling data in the old and new temperature intervals, stress, strain, and HFL show an increasing trend, with the average increasing by 1.47×10^{13} Pa, 1,519.49, and 1.18×10^{6} w/m^2. The growth of strain reaches 5.40~8.90 times (nonlinear mutation of strain) (Fig. 11(c)). Displacement shows a decreasing trend, with an average decreasing rate of 5.88% (Fig. 11(d)).

4.3.2 Analysis of 33# (interval of new time)

Seventy groups of the temperature thermal stress coupling data of the 33# central tower are monitored. According to the conclusion in 4.2.2, the consolidation between the top of the tower and the girder is mainly monitored. The data obtained are as follows. Stress: 346108 > 122112 > 346255 > 346740 > 346230 > 354758 > 346757 > 346627 > 346014 > 356603 (Figs. 12(a),(c)). The central tower is a heat-stress concentrated conduction medium. The last two groups (346014 and 356603) of the ten groups of monitoring points are located at the pile foundation of the central tower (Fig. 10). The heat flux is analysed through the highest and lowest thermal stress losses:

$$\sum \alpha^{m}_{354758} = \frac{\sum(\alpha_{346108}-\alpha_{354758})}{\sum(H_{346108}-H_{354758})} = \frac{2.91921E+13-5.53045E+12}{139.0011-(-39.9278)} = 132{,}240{,}276{,}025.79\text{Pa/m} = 1.32\times10^{11}\text{Pa/m}.$$

$$\sum \alpha^{m}_{356603} = \frac{\sum(\alpha_{346108}-\alpha_{356603})}{\sum(H_{346108}-H_{356603})} = \frac{2.91921E+13-4.26422E+12}{139.0011-(-16.153)} = 160{,}665{,}055{,}416.67\text{Pa/m} = 1.61\times10^{11}\text{Pa/m}.$$

The thermal stress loss per unit area (transverse cutting central tower) is:

$$\sum K^{m}_{354758} = \frac{\sum \alpha^{m}}{\sum S_c} = \frac{1.3224E+11}{69.2} = 1{,}910{,}986{,}647.77\text{Pa·m} = 1.91\times10^{9}\text{Pa·m}.$$

$$\sum K^{m}_{356603} = \frac{\sum \alpha^{m}}{\sum S_c} = \frac{1.6067E+11}{69.2} = 2{,}321{,}749{,}355.73\text{Pa·m} = 2.32\times10^{9}\text{Pa·m}.$$

The conclusions show that: the thermal stress loss is 354758 and the unit heat flux loss is less than 356603, which are linear.

Displacement: 346255 > 6722 > 346108 > 346740 > 346992 > 6739 > 346230 > 346757 > 347093 > 347074 (Figs. 12(a),(c)). The maximum displacement of thermal stress in the two temperature intervals is still maintained at the top of the central tower, and the latter is concentrated at the top of the right central tower (32#→34# is the positive direction) (Fig. 10).

Strain: 346255 > 346108 > 346740 > 354758 > 346757 > 330438 > 2494 > 346627 > 346014 > 356603 (Figs. 12 (b),(c)). HFL: 346255 > 330485 > 346108 > 346014 > 347070 > 345717 > 2517 > 347074 > 273 > 2511 (Figs. 12 (b),(c)). The heat flux field is concentrated in three areas: the tower top of the tower (the highest one is 1.7 times the beam tower consolidation), the second row of cross beams of the central tower (top of the tower → pile foundation direction), and the consolidation of the tower, beam, and pier (Fig. 10).

The study compared the thermal stress coupling data of the 33# central tower at two temperature intervals (0□ ~ 39□; 1□ ~ 38□). The results show a downward trend in stress, with a decrease of 19.78%. The displacement decreased slightly by only 3.88% compared to the original data. There is also a decreasing trend in strain, which is 32.03% lower than the original data. However, there was a significant difference in HFL. The first six monitoring points showed a decrease of 60.95%, while the last four groups showed an increase of 12.70%. Among the ten data groups, the change in stress is significant, with a range of 0.95 to 4.88. On the other hand, the change in displacement is consistent and fluctuates within a small range of 0.96 (Fig. 12(d)).

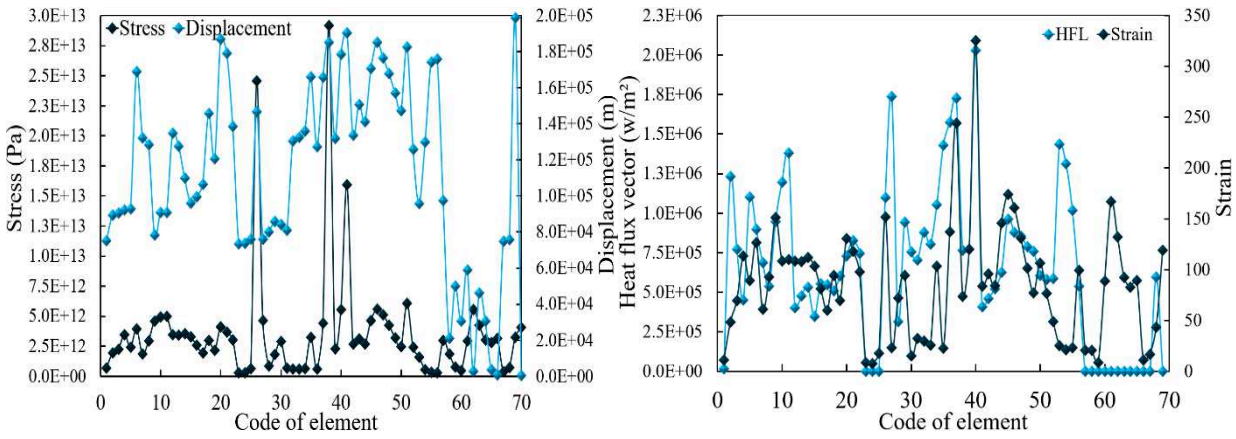

(a) (b)

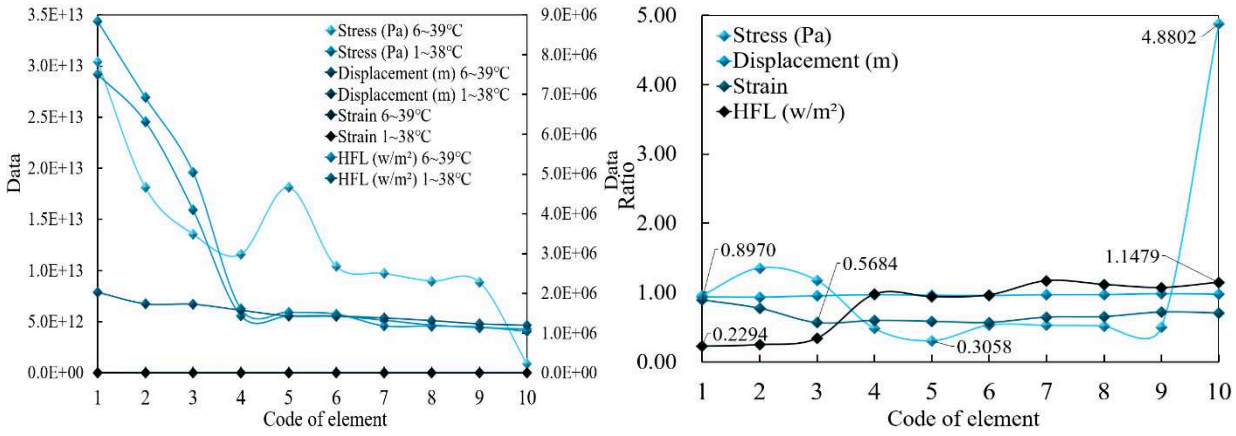

(c) (d)

Fig. 12. Thermal coupling design analysis (33#). (a) Data comparison of S-D; (b) Data comparison of S-H; (c) Comparison of thermomechanical coupling data at two temperatures; (d) Ratio of elements.

4.3.3 Analysis of 32~34# (interval of new time)

The 32# and 34# central piers have a uniaxial compressive strength of 80~100MPa and are supported by a pile foundation inserted directly into the underground rock to a depth of 4m. This provides reasonable constraints on the nonlinear elastic and plastic deformation caused by ambient temperature coupling stress (Razmi and McCabe, 2020). The interface between the bearing, main pier, bearing platform, and pile foundation is the primary focus area for monitoring, with 41 monitoring points. The collected data is presented below.

Stress: 5108 > 5104 > 2226 > 238 > 574 > 2227 > 350789 > 246 > 7744 > 2365 (Figs. 13(a),(c)). Among the ten groups of monitoring points, 32# account for six groups, 34# account for four groups, and 80% of the monitoring points are distributed at the support and the girder. The monitoring point 350789 is in the middle of the 32# pile foundation; the monitoring point 2365 is on the upper surface of the 32# bearing platform (Fig. 10). The conclusion is consistent with that in 4.2.3, verifying the robustness of the analysis of the solar orbit in Fig. 3.

Displacement: 351729 > 350789 > 262 > 2365 > 330342 > 427576 > 351611 > 2251 > 330229 > 330034 (Figs. 13(a),(c)). Ten groups of monitoring points are all in the area of 32#. Strain: 5108 > 574 > 5104 > 246 > 238 > 2365 > 2288 > 351720 > 352314 > 2227 (Figs. 13(b),(c)). The distribution ratio of monitoring points in 32# and 34# is 6:4, and the high strain point 5108 is located at 34#.

HFL: 5104 > 2365 > 5108 > 233 > 393392 > 242 > 2227 > 262 > 7828 > 1030 (Figs. 13(b),(c)). The distribution ratio of monitoring points is 1:1.

When comparing parameters changes between two temperature regions, the results show that stress exhibits a decreasing trend with an average decrease of 16.67%. As for displacement, the first four monitoring points show an increased rate of 1.80%, while the last six groups of monitoring points exhibit a decrease rate of 8.60%, leading to a comprehensive decrease of 4.20%. Strain exhibits a decreasing trend with a maximum decreasing rate of 18.55%. The HFL shows a high decreasing rate of 30.09%, making it the parameter with the most significant change interval (0.464 ~ 1.000) and consistent with the analysis conclusion (Fig. 13(d)). Among the four parameters, HFL exhibits the most significant change.

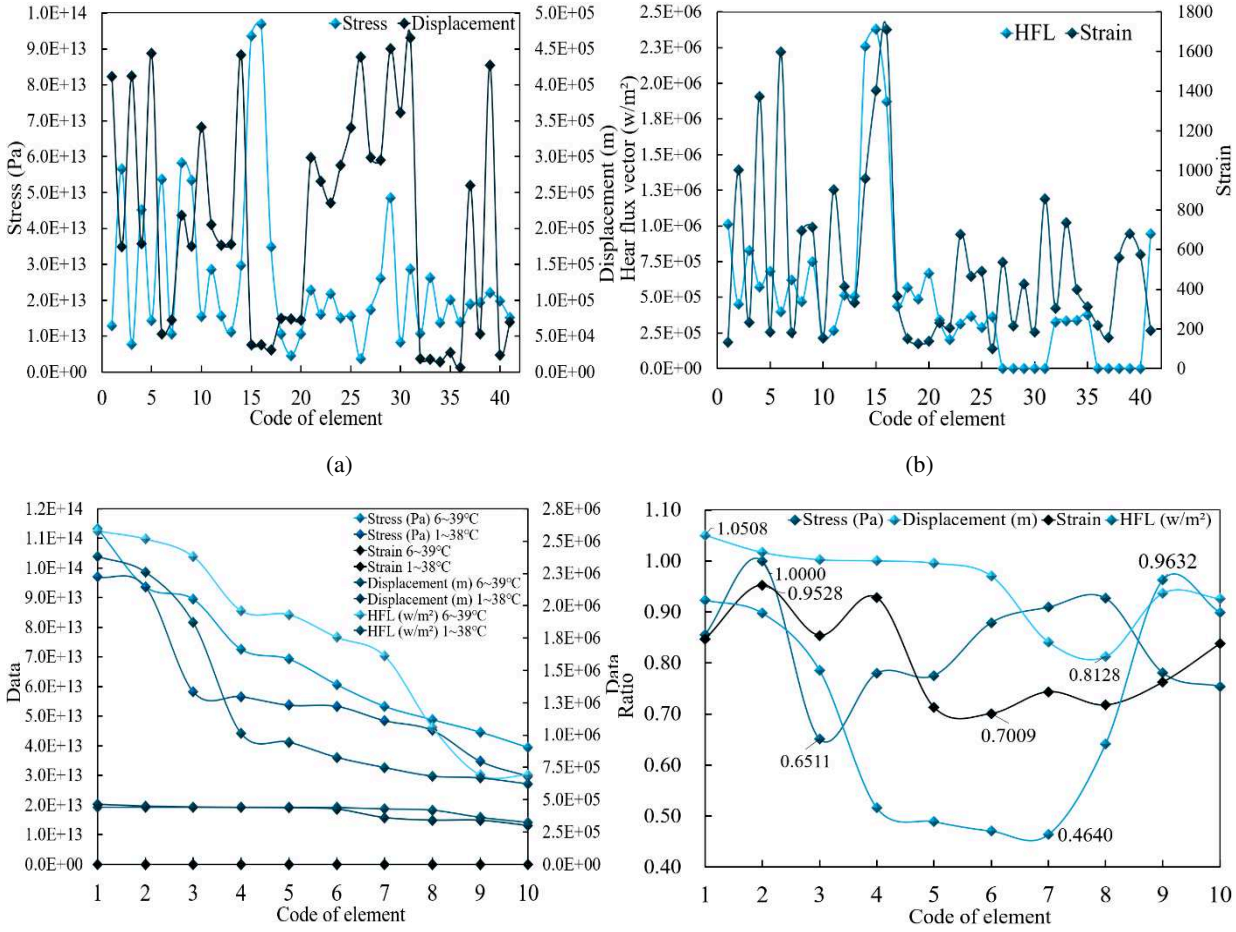

Fig. 13. Thermal coupling design analysis (32#~34#). (a) Data comparison of S-D; (b) Data comparison of S-H; (c) Comparison of thermomechanical coupling data at two temperatures; (d) Ratio of elements.

4.3.4 Analysis of stay-cable # (interval of new time)

Based on the data analysis in section 4.2.2, it is revealed that the stay cable is the most crucial component of JGZB that is affected by temperature thermal stress coupling. The monitoring was conducted on 157 groups of points; the recorded data are presented below. The stress levels are listed in descending order: 255695, 257362, 178012, 175263, 265070, 263726, 184246, 184861, 271605, and 272696 (Fig. 14(a)). These ten groups of monitoring points are all located in the 32# to 33# right stay cables (Fig. 10).

Displacement: 264639 > 184246 > 255947 > 192976 > 265070 > 175263 > 315230 > 268767 > 255695 > 234492 (Fig. 14(a)). The distribution is the same as that of stress.

Strain: 257362 > 14998 > 257866 > 265304 > 270339 > 28184 > 186056 > 184861 > 270045 > 265070 (Fig. 14 (b)). The two groups of monitoring points (14998 and 28184) are distributed in the 33#~34# right stay cables (Fig. 10), and the distribution of the others is the same as the stress. HFL: 179128 > 187700 > 160276 > 183265 > 268220 > 263726 > 272696 > 151781 > 234097 > 30224 (Fig. 14(b)). The two monitoring points with the highest data are concentrated on the top of the tower, and other monitoring points are distributed discretely.

The analysis results show that stress and HFL are decreased, with a decrease rate of 4.84% and 3.33%. Displacement and strain are increased, with an increased rate of 1.74% and 2.08%, respectively. The maximum data change interval is stress (0.764~0.999) (Figs.14(c), (d)).

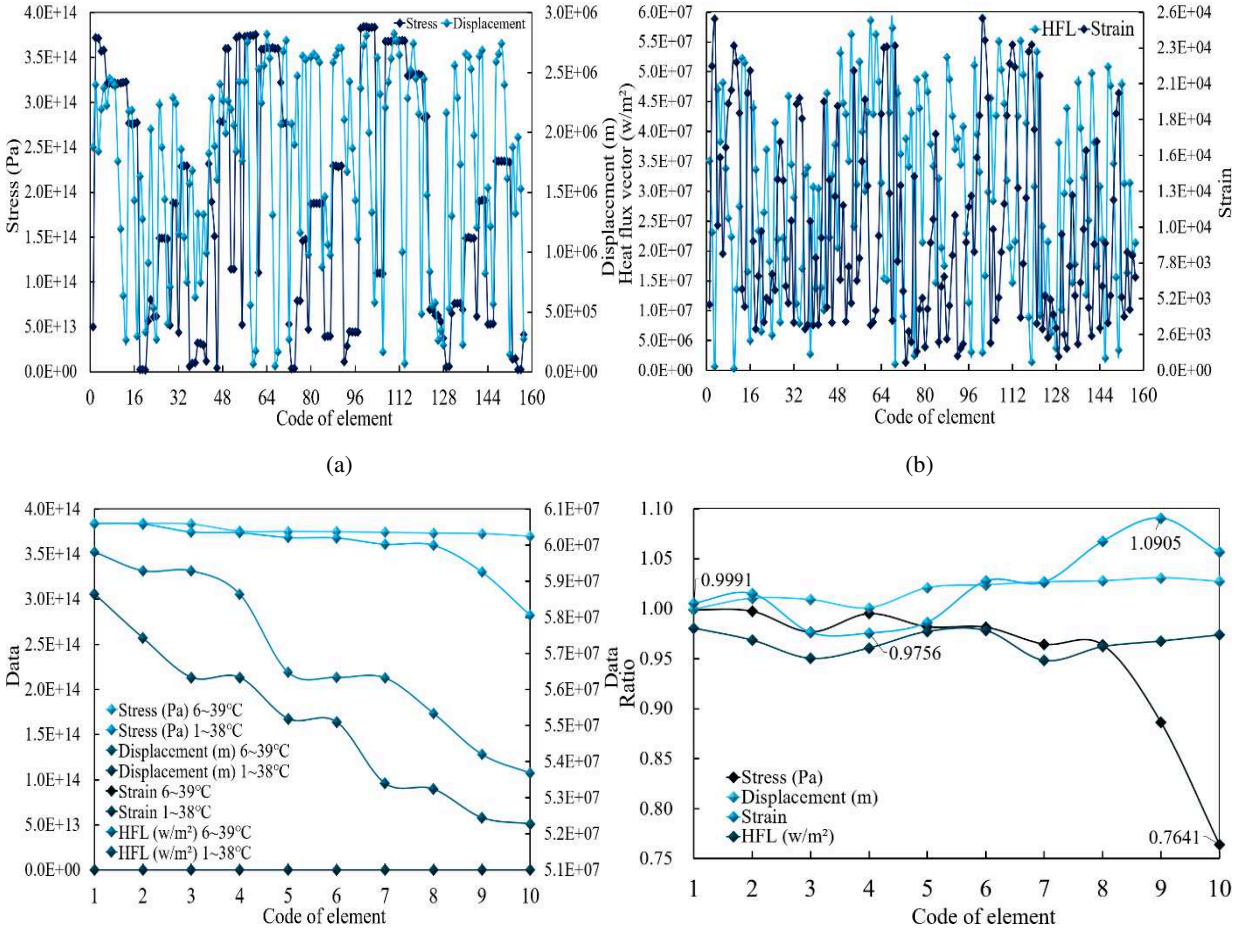

Fig. 14. Thermal coupling design analysis (stay-cable). (a) Data comparison of S-D; (b) Data comparison of S-H; (c) Comparison of thermomechanical coupling data at two temperatures; (d) Ratio of elements.

4.3.5 Analysis of sensitivity (interval of new time)

According to 3.1.3, the research model and analysis data established and obtained in 4.2.3 are used to calculate the α_x value in the temperature interval of 1□~38□, and the components' first ten groups of monitoring points are selected.

$\alpha_{\text{Girder bottom}} = 5.8349\times10^{30} \sim 4.3334\times10^{29}$; $\alpha_{33\#} = 3.6694\times10^{27} \sim 1.1766\times10^{26}$; $\alpha_{32\#\sim34\#} = 1.8402\times10^{29} \sim 3.9499\times10^{27}$; $\alpha_{\text{Stay cable}} = 1.6263\times10^{33} \sim 8.8955\times10^{32}$.

Table 3

Sensitivity data after thermal stress coupling analysis in different temperature ranges.

Code	Girder bottom		33#		32#-34#		Stay-cable	
TE	DT (10^{28})	MT (10^{28})	DT(10^{26})	MT(10^{26})	DT(10^{28})	MT(10^{28})	DT(10^{33})	MT(10^{33})
1	94.20	583.00	198.00	36.70	26.20	18.40	1.65	1.63
2	51.30	412.00	78.90	19.50	17.50	15.20	1.60	1.58
3	313.00	276.00	40.60	8.86	15.50	6.79	1.55	1.42
4	7.04	189.00	9.94	2.73	9.31	3.48	1.48	1.38
5	6.52	110.00	14.40	2.34	8.29	2.23	1.38	1.33
6	5.03	68.90	7.65	2.15	6.42	1.81	1.30	1.32
7	4.04	60.10	4.92	1.91	4.49	1.18	1.29	1.24

8	2.98	54.70	4.26	1.57	2.60	0.90	1.21	1.23
9	2.48	50.60	3.46	1.32	1.09	0.58	1.13	1.09
10	2.16	43.30	0.30	1.18	0.75	0.40	1.10	0.890

Notes: Temperature = TE; Design temperature (0□~39□) = DT; Monitor temperature (1□~38□) = MT.

Table 3 presents sensitivity data for JGZB under two temperature intervals. The bottom boundary girder has a correlation data of 57.49%, indicating that the thermal stress of the ambient temperature field is lower than that of the design temperature field. The 33# boundary girder has a correlation data of 556.92%, indicating that the thermal stress of the ambient temperature field is higher than that of the design temperature field. For the 32#~34# boundary girder, the correlation data is 141.09%, indicating that the thermal stress of the ambient temperature field is also higher than that of the design temperature field. In the case of the stay cable, the correlation data is 74.73%, indicating that the thermal stress of the ambient temperature field is lower than that of the design temperature field.

4.3.6 Analysis of resilience damage

The elastic damage model of lattice elements was established in 3.3, and the finite element mesh model is regarded as an elastic coupling model composed of multiple lattices (Tompkins et al., 2015). After transformation, Eq (14) is used to analyse the damage parameters of the girder and stay cable of JGZB:

$$\alpha^m = (1-\delta)\times\theta\times\varepsilon \rightarrow \delta = 1-\frac{\alpha^m}{\theta\times\varepsilon} \rightarrow \sum\delta = 1-\frac{\sum\alpha^m}{\theta\times\varepsilon} \tag{17}$$

θ is the elastic stiffness, equivalent to the elastic modulus in reinforced concrete structures (in nonlinearly elastic materials) (Kim and Laman, 2013). According to the analysis and calculation: The girder δ is (-0.340,4~0.002,2) under the coupling effect of ambient temperature and thermal stress from 2011 to 2021; $\delta$the stay cable is (0.927,1~0.938,4) (Table 4).

Table 4

Data after damage model analysis (the first ten groups of monitoring points).

Code	1	2	3	4	5	6	7	8	9	10
Girder (bottom)	-0.3404	-0.1422	-0.5720	-0.5872	-0.2232	-0.0968	-0.1625	-0.1189	-0.0643	0.0022
Stay cable	0.9271	0.9271	0.9242	0.9233	0.9244	0.9242	0.9254	0.9254	0.9307	0.9384

Notes: A negative value indicates that the service life of the structure is prolonged, and a positive value indicates that the service life of the structure is shortened.

4.4 Discussion

Section 4 analyzes the thermal coupling model of the bridge under two ambient temperatures and obtains accurate parameters for structural damage. During maintenance, the life cycle assessment (LCA) is analyzed according to the service life specified in the Chinese bridge design code. The data must be consistent with the design drawings and are analyzed using OpenLCA 1.10 software. In addition, Zhou et al. (2020) discuss the replacement years of components in the sustainable study of cable-stayed bridges, which is also relevant to this bridge.

Table 5

Maintenance data of JGZB.

Component name	Maintenance cycle	Start-End time	Cycles of design	Damage factor	Cycles of optimization
Girder	Replacement/50 years	2000~2099 year	2.00	-0.2305	1.6254
Stay-cable	Replacement/20 years	2000~2099 year	5.00	0.9270	5.3937
Basin type rubber bearing	Replacement/25 years	2000~2099 year	4.00	Normal	4.0000

Expansion joint, Anti-collision guardrail	Replacement/15 years	2000~2099 year	6.70	Normal	6.7000
Waterproof layer, Bridge deck paving	Replacement/10 years	2000~2099 year	10.00	Normal	10.0000

The design quantities and data from Table 5 are input into open LCA software, which generates 23,046 processes and 414,148 process links. The analysis results for valid items are presented in Table 6: JGZB releases a total of 2,621.30 million t during the 100-year maintenance period, with marine aquatic ecotoxicity accounting for 99.805%, human toxicity accounting for 0.132%, freshwater aquatic ecotoxicity accounting for 0.038%, and global warming potential (GWP100) accounting for 0.022%. Emissions from other sources are relatively low.

Table 6

LCA data of JGZB analysed according to design specification (within 100-year maintenance period)

Code	Indicator	Unit（(Index: eq)）	Number
1	Abiotic depletion	kg Sb	3,730,000.0
2	Acidification	kg SO2	7,260,000.0
3	Eutrophication	kg PO4	3,910,000.0
4	Fresh water aquatic ecotax	kg 1,4-DB	1,020,000,000.0
5	Global warming (GWP100)	kg CO2	573,000,000.0
6	Human toxicity	kg 1,4-DB	3,470,000,000.0
7	Marine aquatic ecotoxicity	kg 1,4-DB	2,620,000,000,000.0
8	Ozone layer depletion (ODP)	kg CFC-11	33.0
9	Photochemical oxidation	kgC2H4	346,000.0
10	Terrestrial ecotoxicity	kg 1,4-DB	11,900,000.0

The maintenance cycle of the girders and stay cables is re-evaluated based on the data in Table 4 and Section 4.3.5. Interpolation is applied to compute and analyze the data in Table 5. As a result, the replacement cycle of the girders is prolonged to 1.625,4 due to a negative damage coefficient, while the replacement cycle of the stay cables is shortened to 5.393,7 due to a shortened service life. Based on the analysis conclusion, the engineering data during the maintenance period is adjusted, and a new LCA is carried out.

The research conclusions are outlined below: following the optimization, based on LCA, JGZB's emissions have reduced to 2,571.378 million t, representing a decrease of 49.925 million t or 1.91% compared to the original total emissions. Specifically, reducing marine aquatic ecotoxicity amounts to 4,991 million t and freshwater aquatic ecotax by 0.996 million t. The reduction in global warming (GWP100) and human toxicity amounts to 0.279 million t and 0.234 million t, respectively (refer to Fig.15 for details).

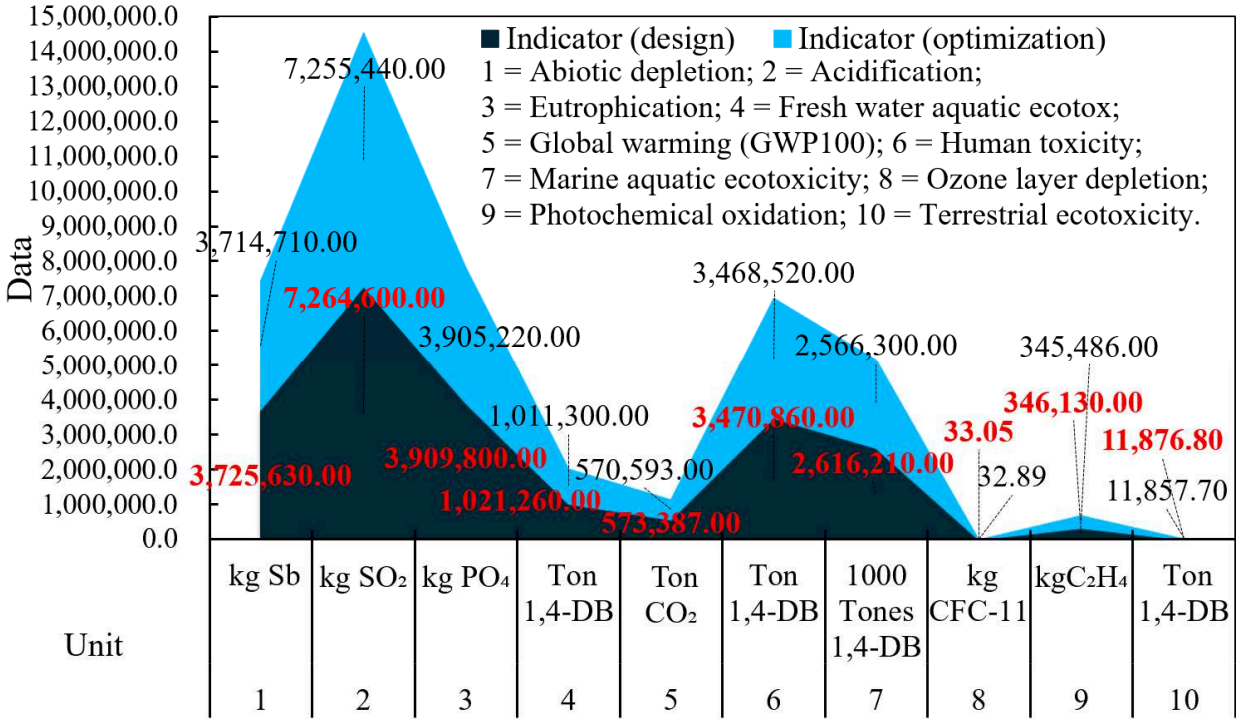

Fig. 15. LCA data comparison of JGZB (design and optimization).

5. Conclusions

As the impact of climate and ambient temperature on the construction industry becomes a critical concern during the maintenance phase of structures, researchers are searching for more effective ways to reduce environmental pollution. This study utilized a 3D analysis to optimize temperature thermal stress coupling under two boundary conditions: standard design ambient temperature and natural climate ambient temperature. The sensitivity data of various components of JGZB was obtained and compared, revealing that the thermal stress of the design temperature field for the girder and stay cable does not align with the ambient temperature field. However, the thermal stress of specific design temperature fields met the ambient temperature field. The damage parameters of the girder and stay cable were obtained using a multi-lattice elastic coupling model. LCA change data of JGZB during the 100-year maintenance period under the natural ambient temperature were reassessed according to the damage parameters, obtaining a reduced emission of 2,571.377 million t after optimization, with a decrease in global warming of 0.279 million t.

Despite providing valuable insight into the impact of ambient temperature on bridge structures, the study has some limitations. It does not consider the variability of future changes in ambient temperatures, such as fluctuations caused by exceptional weather events like hurricanes, fires, and explosions. Additionally, the research only covers the static and dynamic aspects of the temperature's impact and does not consider the cumulative effects over the entire lifespan of the bridge.

The study's theoretical model and high-resolution 3D finite element analysis provide a comprehensive understanding of the coupling between temperature and the mechanical properties of bridge components. Future research could focus on examining the effects of sudden temperature changes on the service life of structures and conducting a discrete analysis of the cumulative impact of ambient temperature on the entire life cycle of a bridge. This research has the potential to pave the way for more effective approaches to mitigating environmental pollution and enhancing the sustainability of bridge structures.

Author contributions

Declaration of competing interest

Acknowledgements

References

Achenbach, J.D., 2014. A new use of the elastodynamic reciprocity theorem. Math. Mech. Solids 19, 5–18. https://doi.org/10.1177/1081286513505462.

Atmaca, B., Ghafoori, R., Dede, T., Ateş, Ş., 2022. The effect of post-tensioning force and different cable arrangements on the behavior of cable-stayed bridge. Structures 44, 1824–1843. https://doi.org/10.1016/j.istruc.2022.08.105.

Balbay, A., Esen, M., 2013. Temperature distributions in pavement and bridge slabs heated by using vertical ground-source heat pump systems. Acta Sci. Technol. 35, 677-685. https://doi.org/10.4025/actascitechnol.v35i4.15712.

Briseghella, B., Fenu, L., Lan, C., Mazzarolo, E., Zordan, T., 2013. Application of Topological Optimization to Bridge Design. J. Bridg. Eng. 18, 790–800. https://doi.org/10.1061/(ASCE)BE.1943-5592.0000416.

Carvalho, J.P., Bragança, L., Mateus, R., 2019. Optimising building sustainability assessment using BIM. Autom. Constr. 102, 170–182. https://doi.org/10.1016/j.autcon.2019.02.021.

Chen, J., Zhao, Q., Zhang, L., 2022. Multi-Material Topology Optimization of Thermo-Elastic Structures with Stress Constraint. Mathematics 10, 1216. https://doi.org/10.3390/math10081216.

Deraemaeker, A., Worden, K., 2018. A comparison of linear approaches to filter out environmental effects in structural health monitoring. Mech. Syst. Signal Process. 105, 1–15. https://doi.org/10.1016/j.ymssp.2017.11.045.

Derdouri, A., Wang, R., Murayama, Y., Osaragi, T., 2021. Understanding the Links between LULC Changes and SUHI in Cities: Insights from Two-Decadal Studies (2001–2020). Remote Sens. 13, 3654. https://doi.org/10.3390/rs13183654.

Dräger, P., Letmathe, P., 2022. Value losses and environmental impacts in the construction industry – Tradeoffs or correlates? J. Clean. Prod. 336, 130435. https://doi.org/10.1016/j.jclepro.2022.130435.

Fu, L., Sun, Z., Zha, L., Liu, F., He, L., Sun, X., Jing, X., 2020. Environmental awareness and pro-environmental behavior within China's road freight transportation industry: Moderating role of perceived policy effectiveness. J. Clean. Prod. 252, 119796. https://doi.org/10.1016/j.jclepro.2019.119796.

Griffiths, D. V., Mustoe, G.G.W., 2001. Modelling of elastic continua using a grillage of structural elements based on discrete element concepts. Int. J. Numer. Methods Eng. 50, 1759–1775. https://doi.org/10.1002/nme.99.

He, J., Xin, H., Wang, Y., Correia, J.A.F.O., 2021. Effect of temperature loading on the performance of a PC bridge in Oklahoma: Reliability analysis. Structures 34, 51–60. https://doi.org/10.1016/j.istruc.2021.06.099.

Huang, H. xin, Zhang, Z., Han, li zhong, 2006. Time domain analysis on buffeting of Jin ma a bridge. Journalof chong qing jianzhu Univ. 28, 63–66. https://www.researchgate.net/publication/291900085_Time_domain_analysis_on_buffeting_of_Jinma_bridge.

Jayaseelan, H., Russell, B.W., Webb, A.C., 2019. Early Age Deflections in Newly Rehabilitated Steel Girder Bridges Made Composite with Concrete Slabs. Struct. Eng. Int. 29, 575–585. https://doi.org/10.1080/10168664.2019.1605326.

Kim, W., Laman, J.A., 2013. Integral Abutment Bridge behavior under uncertain thermal and time-dependent load. Struct. Eng. Mech. 46, 53–73. https://doi.org/10.12989/sem.2013.46.1.053.

Kutylowski, R., Rasiak, B., 2014. The use of topology optimization in the design of truss and frame bridge girders. Struct. Eng. Mech. 51, 67–88. https://doi.org/10.12989/sem.2014.51.1.067.

719 Lee, J., Loh, K.J., Choi, H.S., An, H., 2019. Effect of Structural Change on Temperature Behavior of a Long-Span
720 Suspension Bridge Pylon. Int. J. Steel Struct. 19, 2073–2089. https://doi.org/10.1007/s13296-019-00279-3.
721 Li, Q., Long, R., Chen, H., Chen, F., Wang, J., 2020. Visualized analysis of global green buildings: Development,
722 barriers and future directions. J. Clean. Prod. 245, 118775. https://doi.org/10.1016/j.jclepro.2019.118775.
723 Lian, Q., Zhang, P., Li, H., Yuan, W., Dang, X., 2021. Adjustment method of bridge seismic importance factor based
724 on bridge network connectivity reliability. Structures 32, 1692–1700.
725 https://doi.org/10.1016/j.istruc.2021.03.113.
726 Liu, H., Zhang, W., Gao, T., 2016. Structural topology optimization under rotating load. Struct. Multidiscip. Optim.
727 53, 847–859. https://doi.org/10.1007/s00158-015-1356-3.
728 Liu, Y., Zhang, S., 2017. Probabilistic Baseline of Finite Element Model of Bridges under Environmental
729 Temperature Changes. Comput. Civ. Infrastruct. Eng. 32, 581–598. https://doi.org/10.1111/mice.12268.
730 Ma, M., Li, Z., Xue, K., Liu, M., 2021. Exergy-Based Life Cycle Assessment Model for Evaluating the
731 Environmental Impact of Bridge: Principle and Case Study. Sustainability 13, 11804.
732 https://doi.org/10.3390/su132111804.
733 Meng, Q., Xu, B., Wang, C., Zhao, L., 2021. Thermo□elastic topology optimization with stress and temperature
734 constraints. Int. J. Numer. Methods Eng. 122, 2919–2944. https://doi.org/10.1002/nme.6646.
735 Montassar, S., Mekki, O. Ben, Vairo, G., 2015. On the effects of uniform temperature variations on stay cables. J.
736 Civ. Struct. Heal. Monit. 5, 735–742. https://doi.org/10.1007/s13349-015-0140-9.
737 Molina-Moreno, F., García-Segura, T., Martí, J. V., & Yepes, V. 2017. Optimization of buttressed earth-retaining
738 walls using hybrid harmony search algorithms. Engineering Structures, 134, 205–216.
739 https://doi.org/10.1016/j.engstruct.2016.12.042.
740 Navarro, I.J., Yepes, V., Martí, J. V., 2018. Social life cycle assessment of concrete bridge decks exposed to
741 aggressive environments. Environmental Impact Assessment Review, 72: 50-63.
742 https://doi.org/10.1016/j.eiar.2018.05.003.
743 Ozakin, A., Yavari, A., 2010. A geometric theory of thermal stresses. J. Math. Phys. 51, 032902.
744 https://doi.org/10.1063/1.3313537.
745 Penadés-Plà, V., García-Segura, T., Yepes, V., 2019. Accelerated optimization method for low-embodied energy
746 concrete box-girder bridge design. Eng. Struct. 179, 556–565. https://doi.org/10.1016/j.engstruct.2018.11.015.
747 Pham, D.T., Nguyen, T.D., Vu, M.N., Chinkulkijniwat, A., 2021. Mesoscale approach to numerical modelling of
748 thermo-mechanical behaviour of concrete at high temperature. Eur. J. Environ. Civ. Eng. 25, 1329–1348.
749 https://doi.org/10.1080/19648189.2019.1577762.
750 Pons, J.J., Penadés-Plà, V., Yepes, V., Martí, J. V., 2018. Life cycle assessment of earth-retaining walls: An
751 environmental comparison. J. Clean. Prod. 192, 411–420. https://doi.org/10.1016/j.jclepro.2018.04.268.
752 Rahmzadeh, A., Alam, M.S., Tremblay, R., 2021. Experimental Investigations on the Lateral Cyclic Response of
753 Post-Tensioned Rocking Steel Bridge Piers. J. Struct. Eng. 147, 04021211.
754 https://doi.org/10.1061/(ASCE)ST.1943-541X.0003197.
755 Razmi, J., McCabe, M., 2020. Analytical and Computational Modeling of Integral Abutment Bridges Foundation
756 Movement due to Seasonal Temperature Variations. Int. J. Geomech. 20, 04019189.
757 https://doi.org/10.1061/(ASCE)GM.1943-5622.0001622.
758 Sharma, A., Bošnjak, J., Bessert, S., 2019. Experimental investigations on residual bond performance in concrete
759 subjected to elevated temperature. Eng. Struct. 187, 384–395. https://doi.org/10.1016/j.engstruct.2019.02.061.
760 Sun, G., Li, X., Wu, J., Chen, R., Chen, G., 2020. Deformation of stainless steel cables at elevated temperature. Eng.
761 Struct. 211, 110498. https://doi.org/10.1016/j.engstruct.2020.110498.
762 Tompkins, D., Khazanovich, L., Bolander, J.E., 2015. Lattice modelling of fracture in composite concrete pavements

763 and overlays. Int. J. Pavement Eng. 16, 56–68. https://doi.org/10.1080/10298436.2014.893332.
764 Wang, T., Li, H., Ge, Y., 2015. Vertical seismic response analysis of straight girder bridges considering effects of
765 support structures. Earthquakes Struct. 8, 1481–1497. https://doi.org/10.12989/eas.2015.8.6.1481.
766 Wen, P., Ji, K., Wen, R., 2022. Simplified procedure for simulating artificial non-stationary multi-point earthquake
767 accelerograms. Soil Dyn. Earthq. Eng. 156, 107239. https://doi.org/10.1016/j.soildyn.2022.107239.
768 Wu, C., Fang, J., Li, Q., 2019. Multi-material topology optimization for thermal buckling criteria. Comput. Methods
769 Appl. Mech. Eng. 346, 1136–1155. https://doi.org/10.1016/j.cma.2018.08.015.
770 Xia, L., Zhang, L., Xia, Q., Shi, T., 2018. Stress-based topology optimization using bi-directional evolutionary
771 structural optimization method. Comput. Methods Appl. Mech. Eng. 333, 356–370.
772 https://doi.org/10.1016/j.cma.2018.01.035.
773 Xia, Y., Chen, B., Zhou, X., Xu, Y., 2013. Field monitoring and numerical analysis of Tsing Ma Suspension Bridge
774 temperature behavior. Struct. Control Heal. Monit. 20, 560–575. https://doi.org/10.1002/stc.515.
775 Xu, X., Ren, Y., Huang, Q., Zhao, D.-Y., Tong, Z.-J., Chang, W.-J., 2020. Thermal response separation for bridge
776 long-term monitoring systems using multi-resolution wavelet-based methodologies. J. Civ. Struct. Heal. Monit.
777 10, 527–541. https://doi.org/10.1007/s13349-020-00402-7.
778 Yao, R., Hu, Y., Sun, P., Bian, Y., Liu, R., Zhang, S., 2022. Effects of urbanization on heat waves based on the wet-
779 bulb temperature in the Yangtze River Delta urban agglomeration, China. Urban Clim. 41, 101067.
780 https://doi.org/10.1016/j.uclim.2021.101067.
781 Yue, Z., Ding, Y., Zhao, H., Wang, Z., 2022. Mechanics-Guided optimization of an LSTM network for Real-Time
782 modeling of Temperature-Induced deflection of a Cable-Stayed bridge. Eng. Struct. 252, 113619.
783 https://doi.org/10.1016/j.engstruct.2021.113619.
784 Zamarrón-Mieza, I., Yepes, V., & Moreno-Jiménez, J. M. 2017. A systematic review of application of multi-criteria
785 decision analysis for aging-dam management. J. Clean. Prod. 147, 217-230.
786 https://doi.org/10.1016/j.jclepro.2017.01.092.
787 Zhou, Z., Alcalá, J., Yepes, V., 2020. Environmental, Economic and Social Impact Assessment: Study of Bridges
788 in China's Five Major Economic Regions. Int. J. Environ. Res. Public Health 18, 122.
789 https://doi.org/10.3390/ijerph18010122.
790 Zhou, Z.W., Alcalá, J., Yepes, V., 2022. Regional sustainable development impact through sustainable bridge
791 optimization. Structures 41, 1061–1076. https://doi.org/10.1016/j.istruc.2022.05.047.
792 Zu, L., Huang, Y., Li, W., Zhang, H., Cai, L., 2022. Seismic damage analysis of Yematan Bridge under near-fault
793 earthquakes. Structures 41, 586–601. https://doi.org/10.1016/j.istruc.2022.05.006.
794